



1 **Evaluating the EPICC-Model for Regional Air Quality**
2 **Simulation: A Comparative Study with CAMx and CMAQ**

3
4 **Mengjie Lou¹, Qizhong Wu¹, Wending Wang^{2,3,4}, Huansheng Chen^{2,3,4}, Kai Cao²,**
5 **Xiaohan Fan⁵, Dingyue Liang⁵, FenFen Yu⁵, Jiating Zhang¹, Wei Wang⁶, Zifa**
6 **Wang^{2,3,4}**

7
8 ¹Institute of Earth System Science, Faculty of Geographical Science, Beijing Normal
9 University, Beijing, 100875, China

10 ²State Key Laboratory of Atmospheric Environment and Extreme Meteorology,
11 Institute of Atmospheric Physics, Chinese Academy of Sciences, Beijing, 100029,
12 China

13 ³State Key Laboratory of Atmospheric Boundary Layer Physics and Atmospheric
14 Chemistry, Institute of Atmospheric Physics, Chinese Academy of Sciences, Beijing,
15 100029, China

16 ⁴University of Chinese Academy of Sciences, Beijing, 100049, China

17 ⁵3Clear Technology Co., Ltd., Beijing, 100029, China

18 ⁶China National Environmental Monitoring Centre, Beijing, 100012, China

19
20 **Correspondence:** Qizhong Wu (wqizhong@bnu.edu.cn) and Wending Wang
21 (wangwending@mail.iap.ac.cn)
22

23 **Abstract**

24 This study presents a systematic evaluation of China's independently developed
25 EPICC-Model for regional PM_{2.5} and MDA8 O₃ simulations against established
26 international models, using WRF meteorological fields and a multi-source integrated
27 emission inventory. Results highlight the strengths of the EPICC-Model in several
28 aspects: it achieves relatively high spatial consistency with measurements for PM_{2.5},
29 with an annual index of agreement (IOA) of 0.80, and accurately captures pollution
30 patterns in heavily polluted North China. It also demonstrates improved performance
31 in simulating summer O₃ peaks, reducing maximum biases by more than 20 µg m⁻³,
32 primarily through enhanced heterogeneous HONO formation and nitrate photolysis
33 pathways that elevate OH concentrations, and it incorporates the CB6r5 mechanism to
34 better represent biogenic VOC oxidation. The model exhibits the highest hit rate (45.6%)
35 for forecasting moderate PM_{2.5} and moderate O₃ pollution events and successfully
36 reproduces persistent pollution episodes. However, all models share common
37 limitations, including insufficient capability in reproducing heavy pollution episodes,
38 systematic underestimation of SO₄²⁻, and uncertainties in SOA-related OC simulations.
39 Future improvements should focus on refining secondary aerosol chemistry, emission
40 inventories, and boundary layer representations. This study has not only demonstrated
41 the performance of the EPICC-Model against international models but also provides
42 guidance for improving regional and global air quality models.



43 1 Introduction

44 With rapid urbanization and industrialization, China faces increasingly severe
45 multi-pollutant air quality challenges. Among them, fine particulate matter (PM_{2.5}) and
46 ozone (O₃) are key threats to public health and ecosystems, and their coordinated
47 control has become a priority. As a typical secondary pollutant, PM_{2.5} is influenced by
48 primary emissions, secondary formation from SO₂, NO_x, and VOCs, regional transport,
49 and meteorology (Zhang et al., 2012; Jing et al., 2020). Emission control policies have
50 reduced population-weighted PM_{2.5} exposure by ~48% from 2013 to 2020 (Xiao et al.,
51 2022), yet severe winter haze episodes persist in regions like Beijing-Tianjin-Hebei. In
52 contrast, O₃ formation shows nonlinear dependence on NO_x and VOCs and is highly
53 sensitive to radiation, temperature, humidity, and the boundary layer dynamics (Li et
54 al., 2019b; Gao et al., 2022). Despite PM_{2.5} reductions, O₃ levels have risen steadily due
55 to a non-linear response to precursor NO_x reductions, with warm-season maximum
56 daily 8-hour average (MDA8) O₃ increasing by 1.2 ± 1.3 ppb yr⁻¹ in major urban
57 clusters during 2013-2022 (Wang et al., 2024). The combined pollution of PM_{2.5} and O₃
58 exhibits complex spatiotemporal evolution patterns and formation mechanisms (Lyu et
59 al., 2025; Zhu et al., 2023), posing significant challenges for sustained air quality
60 improvement in China.

61 To better understand the formation of complex air pollution and assess control
62 strategies, Chemical Transport Models (CTMs) are widely used for regional air quality
63 analysis and policy evaluation (Li et al., 2021; Gao and Zhou, 2024). Representative
64 CTMs include the Community Multiscale Air Quality Modeling System (CMAQ)
65 developed by the U.S. Environmental Protection Agency (EPA), the Comprehensive
66 Air Quality Model with Extensions (CAMx) developed by Ramboll, WRF-Chem for
67 regional-scale simulations, and GEOS-Chem, which is widely applied for global-scale
68 studies. However, current CTMs still exhibit significant uncertainties in simulating
69 PM_{2.5} and O₃ under specific pollution scenarios in China, primarily manifested as
70 systematic biases in peak concentrations, spatiotemporal distribution errors, and
71 inaccuracies in capturing seasonal variability (Bessagnet et al., 2016; Chen et al., 2019).
72 Against this backdrop, China has independently developed the Emission and
73 atmospheric Processes Integrated and Coupled Community Model (EPICC-Model) to
74 enhance capabilities in simulating complex pollution processes. Supported by the
75 National Natural Science Foundation of China (Major Program) and the Earth System
76 Numerical Simulation Facility (EarthLab), the model was officially released on
77 November 8, 2024 (EPICC-Model Working Group, 2025) (for detailed description, see
78 Section 2.1).

79 As a newly released CTM, the EPICC-Model has undergone preliminary single-
80 model performance evaluations (EPICC-Model Working Group, 2025; Wang et al.,
81 2025), but systematic multi-model comparisons under nationwide, multi-season
82 conditions remain lacking. Multi-model intercomparison not only helps reveal
83 structural differences among models in pollutant transport, chemical reactions, and
84 meteorological feedbacks, but also serves as a key approach to quantifying simulation
85 uncertainties and improving model robustness and reliability (Carmichael et al., 2008).
86 Although substantial efforts have been made in evaluating CTMs over China and East
87 Asia, such as the MICS-Asia phase studies on PM_{2.5} and O₃ (Chen et al., 2019; Gong
88 and Liao, 2019; Itahashi et al., 2020; Li et al., 2019a), regional comparisons in the Pearl
89 River Delta (Wu et al., 2012), and recent multi-model analyses over eastern China (Gao
90 et al., 2024), most focus on earlier-generation or established models. Likewise, large-
91 scale assessments within CMIP5/6 have consistently revealed systematic biases in



92 simulating PM_{2.5} and components across China (Li et al., 2020; Ren et al., 2024). Given
93 the structural innovations and representations in the EPICC-Model, it is both timely and
94 necessary to conduct a systematic comparison with established CTMs over China, in
95 order to comprehensively assess its strengths and weaknesses and provide a scientific
96 basis for subsequent model improvement and application.

97 Therefore, this study implements a consistent model intercomparison framework
98 to systematically compare the simulation performance of three models (EPICC-Model,
99 CMAQ, and CAMx) for PM_{2.5} and O₃ concentrations over China in 2021, based on a
100 unified meteorological driving field and a multi-source integrated emission inventory.
101 The objectives are to comprehensively assess the capabilities of the EPICC-Model,
102 identify common issues and their potential causes across multiple models, and propose
103 targeted improvements. The paper is structured as follows: Section 2 introduces the
104 configuration schemes of the three models, emission data sources, the WRF-based
105 meteorological forcing, and the evaluation of meteorological simulations. Section 3
106 presents the research results, including comparative analyses of the spatiotemporal
107 distribution simulations of PM_{2.5} and O₃, PM_{2.5} chemical composition analysis,
108 assessments of the Air Quality Index (AQI) and pollution forecast accuracy, as well as
109 comparisons of model performance in simulating persistent pollution events. Section 4
110 summarizes the key findings and discusses future directions for model improvements
111 and prospects.

112 **2 Data and methods**

113 **2.1 Overview of simulation domain, period, and CTM configurations**

114 This study employs a two-level nested grid configuration with the model domain
115 centered at (35°N, 105°E). The outer domain covers East Asia with a 45 km horizontal
116 resolution (228 × 165 grid cells), while the inner domain focuses on China at a 15 km
117 resolution (465 × 300 grid cells), starting from grid point (36, 39) within the outer
118 domain. All analyses and results are derived from the inner domain simulations. The
119 simulation period extends from 12:00 UTC on 14 December 2020 to 18:00 UTC on 31
120 December 2021, with the initial 17.25 days (until 18:00 UTC on 31 December 2020)
121 dedicated to model spin-up.

122 For a systematic intercomparison of models, this study employs consistent
123 meteorological driving fields generated by the Weather Research and Forecasting
124 (WRF) model and a harmonized multi-source emission inventory to drive year-long
125 simulations using the EPICC-Model, CAMx, and CMAQ. The EPICC-Model is a three-
126 dimensional tropospheric CTM independently developed in China (EPICC-Model
127 Working Group, 2025). Featuring highly modular architecture and parallel computing
128 capabilities, it simulates key physical and chemical processes including emissions,
129 transport, gas-phase and heterogeneous reactions, aerosol thermodynamics, and
130 dry/wet deposition. CAMx (Ramboll, 2020) is a versatile photochemical grid model
131 widely used for air quality scientific assessments and policy support. It follows the “one
132 atmosphere” approach, accommodating pollution simulations from urban to regional
133 scales (Emery et al., 2024). CMAQ (EPA, 2021) is a continuously evolving open-source
134 modeling platform featuring an open architecture and multi-processor parallel
135 computing capabilities. It efficiently simulates air pollution processes including O₃,
136 particulate matter, toxic pollutants, and acid deposition (US EPA, 2021).



137 **Table 1.** Key configuration schemes of the EPIC-Model, CMAQ, and CAMx.

	EPIC-Model	CAMx	CMAQ
Model version	v1.0	v7.0	v5.3.3
Vertical layers	$20\sigma_z$ layers	$14\sigma_p$ layers	$14\sigma_p$ layers
Horizontal advection	Walcek (Walcek and Aleksic, 1998)	PPM (Colella and Woodward, 1984)	PPM
Vertical advection	Walcek	PPM	PPM
Horizontal diffusion	Multi-scale	Multi-scale	Multi-scale
Vertical diffusion	YSU (Hong et al., 2006)	YSU	ACM2 (Pleim, 2007)
Gas-phase mechanisms	CB6r5 (Yarwood et al., 2020)	CB05 (Yarwood et al., 2005)	CB6r3 (Emery et al., 2015)
Aqueous-phase chemistry	RADM (Walcek and Taylor, 1986)	RADM	AQCHEM
Aerosol processes	ISORROPIA v2.2 (Fountoukis and Nenes, 2007)	CF/ISORROPIA v1.7 (Nenes et al., 1998)	AE7/ISORROPIA v2.2
Secondary organic aerosol	Two-product model (Pandis et al., 1992; Odum et al., 1997)	SOAP2.2 (Ramboll, 2020)	AE7/VBS
Dry deposition	ZHANG03 (Zhang et al., 2001, 2003)	ZHANG03	M3DRY
Wet deposition	Henry's law (William, 1803)	Henry's law	AQCHEM
Photolysis	Streamlined TUV and full-science TUV (Emery et al., 2010; NASA, 2024)	Streamlined TUV and full-science TUV	Fast-J (Wild et al., 2000)
Boundary conditions	MORZART	Default	Default

138 The key configuration parameters of the EPIC-Model, CAMx, and CMAQ are
 139 summarized in Table 1. The EPIC-Model employs a $20\sigma_z$ layers coordinate system,
 140 demonstrating superior vertical resolution compared to the $14\sigma_p$ layers coordinates
 141 used in other two models. Coupled with the YSU boundary layer scheme, this
 142 configuration enhances simulation accuracy for near-surface turbulent mixing and
 143 nocturnal stable layer structures. CMAQ utilizes the Asymmetric Convective Model,
 144 version 2 (ACM2) scheme, which exhibits stronger coupling with surface heat flux
 145 feedback mechanisms, particularly advantageous for simulating boundary layer
 146 evolution under environments with pronounced diurnal temperature gradients. CAMx
 147 retains the YSU scheme, maintaining an optimal balance between computational
 148 efficiency and precision (Jia and Zhang, 2020; Shi et al., 2021). In terms of chemical
 149 mechanisms, the EPIC-Model employs the CB6r5 gas-phase mechanism coupled with
 150 RADM aqueous-phase chemistry, allowing the representation of gas-aqueous reactions
 151 contributing to secondary organic aerosol (SOA) formation, particularly under high-
 152 humidity conditions where aqueous-phase reactions can influence SOA production



153 (Yarwood et al., 2020). CMAQ uses the CB6r3 mechanism in combination with the
 154 AE7/VBS module to represent SOA formation, and from version 5.2 onward,
 155 incorporates additional parameterizations such as Potential Combustion SOA (PCSOA)
 156 to compensate for combustion-related SVOC and IVOC emissions not captured in
 157 current inventories (Murphy et al., 2017). CAMx uses the CB05 gas-phase chemical
 158 mechanism coupled with the SOAP module to parameterize SOA formation, simulating
 159 the oxidation of both anthropogenic and biogenic VOCs and their partitioning into the
 160 aerosol phase. For photolysis rate calculations, both the EPIC-Model and CAMx
 161 employ the Streamlined TUV scheme to reduce computational cost, whereas CMAQ
 162 utilizes the Fast-J scheme, which offers more detailed representation of radiative
 163 shielding under high aerosol loading conditions (Barnard et al., 2004). Regarding
 164 boundary conditions, the EPIC-Model incorporates MOZART outputs as the initial
 165 and lateral background fields, while CMAQ and CAMx rely on their respective default
 166 settings. These differences in physical parameterizations and chemical mechanisms
 167 constitute a critical foundation for interpreting the divergent simulation results of PM_{2.5}
 168 and MDA8 O₃ across the three models.

169 2.2 WRF model configuration and meteorological simulation evaluation

170 Key configuration parameters of the WRF model used in this study are
 171 summarized in Table 2. The simulations were conducted using WRF version 3.9.1, with
 172 initial and boundary conditions derived from the National Centers for Environmental
 173 Prediction (NCEP) Final 1° × 1° reanalysis data (FNL, ds083.2), featuring a temporal
 174 resolution of 6 hours. To enhance the accuracy of the WRF simulations, four-
 175 dimensional data assimilation (FDDA) grid nudging was applied during the simulation
 176 process.

177 **Table 2.** Key configuration parameters of the WRF model.

WRF v3.9.1	
Horizontal resolution	45 km-15 km (one-way nested)
Number of sigma levels	30 σ_p layers, with top layer at 50hPa
Longwave Radiation	RRTMG (Iacono et al., 2008)
Shortwave Radiation	RRTMG
Microphysics	Thompson (Thompson et al., 2008)
Land-surface Model	Unified Noah Land Surface Model (Tewari et al., 2004)
Advection	Monotonic transport
Planetary boundary layer (PBL) scheme	YSU (Hong et al., 2006)
Cumulus option	Kain-Fritsch Scheme (Kain, 2004)
Nudging options	FDDA

178 This study systematically evaluated the performance of the WRF model in
 179 simulating surface meteorological fields over mainland China for the year 2021, based
 180 on comprehensive observational data. The evaluation utilized daily observations from
 181 representative stations in 335 cities nationwide (excluding Jiayuguan and Wujiaqu due
 182 to data unavailability), covering key meteorological variables such as 2 m air



183 temperature, 2 m relative humidity, 10 m wind speed, 10 m wind direction, precipitation,
184 and surface pressure. To ensure seasonal representativeness, January, April, July, and
185 October were selected to represent winter, spring, summer, and autumn, respectively,
186 for comparative analysis (see Fig. S1- Fig. S24 and Supplementary Material for details,
187 including the evaluation metrics).

188 The evaluation results indicate that the WRF model accurately captures the diurnal
189 variations of key meteorological variables across most regions. For 2 m temperature
190 simulations, the Pearson correlation coefficient (R) exceeds 0.7 in January and October,
191 with the Root Mean Square Error (RMSE) below 5 °C and the Mean Bias (MB)
192 constrained within ± 2 °C in North, East, and South China. Simulations of 2 m relative
193 humidity also performed well, with R values generally above 0.7 and RMSE below 15%
194 in April and July; MB values in East and South China were less than $\pm 9\%$. However,
195 relatively large humidity biases were observed in parts of Southwest and Northwest
196 China, where MB in the southwest exceeded 15% and RMSE surpassed 17%. Previous
197 studies suggest that simulations can be considered reliable when $R \geq 0.6-0.7$, RMSE
198 for temperature ≤ 5 °C, and RMSE for humidity $< 15\%$ (Lou et al., 2025; Oyegbile et
199 al., 2024). Therefore, the WRF model used in this study demonstrates high reliability
200 in simulating temperature and humidity. Simulations of 10 m wind speed showed
201 consistent performance, with R exceeding 0.7 and RMSE below 8 m/s in most regions.
202 Nevertheless, systematic overestimations were observed in the Sichuan Basin, Xinjiang,
203 and parts of Tibet. Although the wind speed RMSE exceeds typical values reported in
204 some studies (4-6 m s⁻¹), it remains within an acceptable range given the seasonal
205 variability at the national scale (Xu et al., 2020; Yu et al., 2022b). In contrast, the
206 performance for 10 m wind direction was relatively poor, with R values below 0.4 in
207 most areas, except for moderate improvement in the Beijing-Tianjin-Hebei region, East
208 China, Central China, and South China. This finding aligns with previous research
209 noting WRF's general limitations in reproducing wind direction (Jiménez and Dudhia,
210 2013). For precipitation, correlation coefficients were generally above 0.4 nationwide.
211 However, substantial errors were observed in parts of Southwest, Northwest, and South
212 China, especially in regions with complex terrain, consistent with previous findings (Yu
213 et al., 2022a). Surface pressure simulations exhibited high consistency, with R values
214 exceeding 0.7 across the country. While parts of Southwest and Central China exhibited
215 slight underestimation (MB < 20 hPa), surface pressure was slightly overestimated in
216 Guizhou and Chongqing. Overall, the WRF model provides reliable meteorological
217 forcing fields for CTMs.

218 **2.3 Emission inventory and observational data sources**

219 The anthropogenic emissions data used in this study for China are derived from
220 the Multi-resolution Emission Inventory for China (MEIC) developed by Tsinghua
221 University, with a base year of 2019 (Geng et al., 2024). This inventory includes major
222 source sectors such as transportation, industry, power generation, and residential
223 combustion, and covers multiple pollutants including CO, SO₂, NO_x, VOCs, PM₁₀,
224 PM_{2.5}, BC, and OC. Emissions of ammonia over China are obtained from the PKU-
225 NH₃ inventory (Huang et al., 2012a; Kang et al., 2016), while emissions from biomass



226 burning are taken from the “China Open Biomass Burning Emissions Inventory” with
227 a base year of 2017 (Huang et al., 2012b; Song et al., 2009). The EDGAR v5.0 dataset
228 (Crippa et al., 2020), with a base year of 2015 and a spatial resolution of $0.1^\circ \times 0.1^\circ$,
229 was used to represent anthropogenic emissions outside China. Biogenic emissions are
230 simulated online using the MEGAN v3.2 model (Guenther et al., 2012). It should be
231 noted that although the base years of the emission inventories do not match the
232 simulation year of this study, the use of inventories from adjacent years remains a
233 common practice in regional air quality modeling, especially in the absence of globally
234 consistent, high-resolution, multi-sector emission datasets for the target year. Under the
235 assumption of no substantial changes in regional climate and socioeconomic activities,
236 such inventories can reasonably represent the emission patterns of the study period
237 (Amnuaylojaroen et al., 2014; Huang et al., 2023; Wang et al., 2023). It is important to
238 clarify that no projection or temporal adjustment of the individual emission inventory
239 data to the 2021 simulation year was performed.

240 All surface observational data used in this study were obtained from the China
241 National Environmental Monitoring Center (CNEMC), including hourly $PM_{2.5}$ and O_3
242 concentrations from 1,644 national monitoring stations across China in 2021 (station
243 distribution shown in Fig. S25). Based on these data, daily average $PM_{2.5}$ concentrations
244 and MDA8 O_3 values were calculated for 337 cities. Additionally, aerosol chemical
245 composition data were obtained from the same source for ten representative cities:
246 Beijing ($116.41^\circ E$, $40.04^\circ N$), Tianjin ($117.21^\circ E$, $39.17^\circ N$), Zhengzhou ($113.73^\circ E$,
247 $34.77^\circ N$), Jinan ($117.06^\circ E$, $36.66^\circ N$), Shanghai ($121.53^\circ E$, $31.23^\circ N$), Nanjing
248 ($118.76^\circ E$, $32.07^\circ N$), Wuhan ($114.37^\circ E$, $30.54^\circ N$), Fuzhou ($119.31^\circ E$, $26.10^\circ N$),
249 Chengdu ($104.09^\circ E$, $30.64^\circ N$), and Chongqing ($106.47^\circ E$, $29.62^\circ N$).

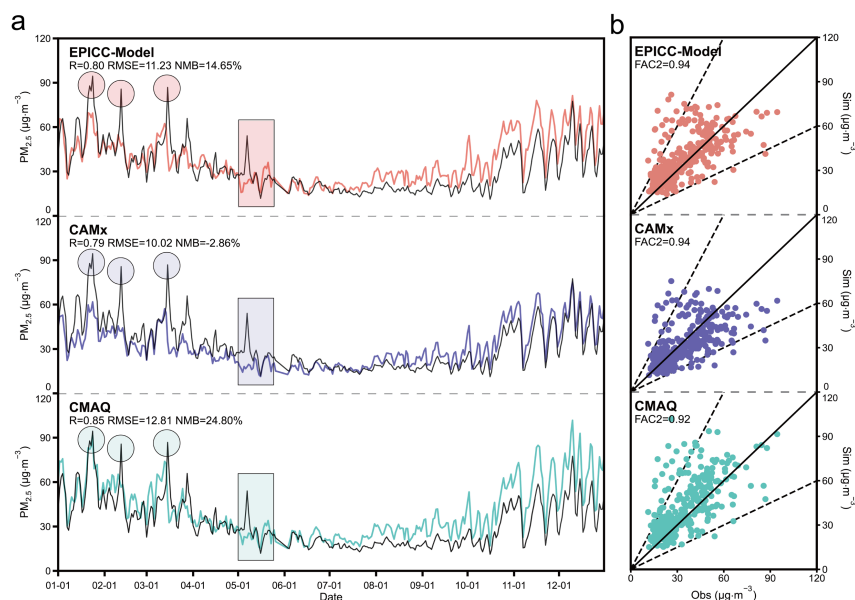
250 **3 Results and discussion**

251 **3.1 Spatiotemporal distribution and statistical analysis of daily averages**

252 Figure 1 presents the performance of the EPIC-Model, CAMx, and CMAQ in
253 simulating annual $PM_{2.5}$ concentrations, evaluated against observations from 1,644
254 national monitoring stations across China. Based on the time series analysis (Figure 1a),
255 the year can be divided into three distinct phases. Phase I (January to mid-May): During
256 this period, both the EPIC-Model and CAMx significantly underestimated $PM_{2.5}$
257 concentrations and failed to capture the three major pollution episodes at the beginning
258 of the year, as indicated by the circles in the figure (with biases ranging from 25 to 52
259 $\mu g m^{-3}$). In contrast, CMAQ showed improved performance in capturing both the timing
260 and intensity of pollution peaks. This was primarily attributed to its substantially higher
261 simulated organic carbon (OC) levels relative to the other models and observations,
262 which produced a compensatory effect on total $PM_{2.5}$ (Figure 6). Additionally, CMAQ
263 exhibited intermittent overestimations during certain periods, which may be related to
264 the ACM2 vertical diffusion scheme it adopts, where the minimum turbulent diffusion
265 coefficient (Kz_{min}) under stable boundary layer conditions is set too low (default
266 nighttime $Kz_{min} = 0.01 m^2 s^{-1}$) (Kim et al., 2024). The contrasting pattern within the
267 rectangular box was attributed to a dust event. Phase II (mid-May to mid-October):



268 During this period, $PM_{2.5}$ concentrations were generally low and exhibited limited
 269 variability. This was primarily attributed to elevated planetary boundary layer heights,
 270 enhanced turbulent mixing, and frequent precipitation events during the summer, which
 271 collectively facilitated the dilution and wet deposition of near-surface particulate matter.
 272 CAMx performed best in this phase. In contrast, both the EPICC-Model and CMAQ
 273 tended to overpredict pollutant levels, with CMAQ exhibiting a notably stronger
 274 positive bias. Phase III (mid-October to December): During the heating season,
 275 observed $PM_{2.5}$ levels increased significantly, accompanied by greater spatiotemporal
 276 variability. CAMx maintained relatively good simulation accuracy during this period,
 277 with smaller biases. However, the overestimation by CMAQ became more pronounced,
 278 which might result from intrinsic biases in its chemical and physical parameterizations,
 279 rather than from differences in emissions or meteorological inputs. The performance of
 280 the EPICC-Model was intermediate between the two.



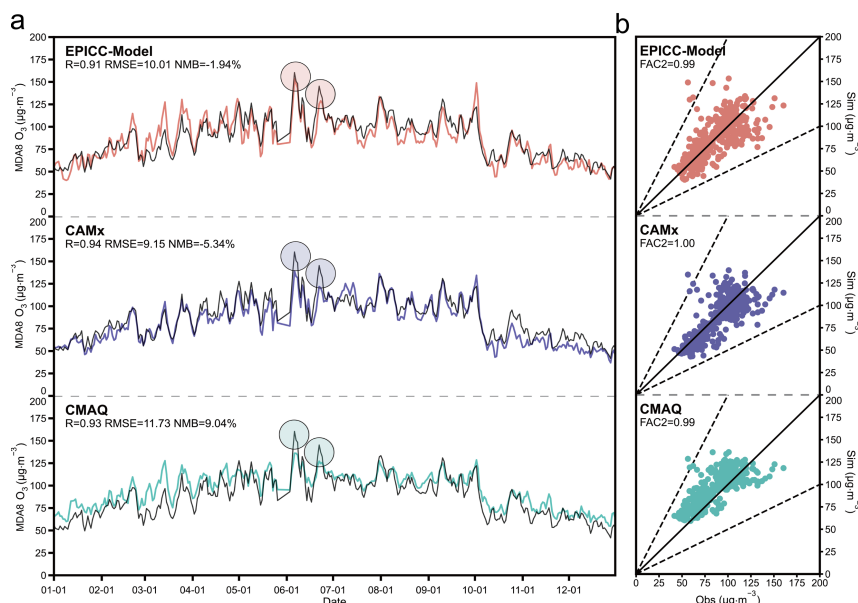
281
 282 **Figure 1.** Comparison of simulated and observed daily $PM_{2.5}$ concentrations across China in 2021.
 283 (a) shows the time series of daily $PM_{2.5}$, with the black line representing observations from 1,644
 284 national air quality monitoring stations and colored lines indicating different CTMs. (b) presents
 285 scatter plots of modeled versus observed $PM_{2.5}$. All model outputs exclude dust aerosol
 286 contributions to isolate secondary particulate formation processes.

287 Statistical validation analysis (Figure 1b) further corroborates the above findings.
 288 Although CMAQ exhibits the highest correlation coefficient (R=0.85), most of its data
 289 points lie above the 1:1 reference line, indicating a systematic overestimation. CAMx
 290 demonstrates the best overall statistical performance, with a Fraction of Predictions
 291 Within a Factor of Two (FAC2) value of 0.94 and a Normalized Mean Bias (NMB) of
 292 merely -2.86%. It is important to note that CAMx struggles to capture severe pollution
 293 episodes, markedly underestimating periods of high concentrations, which constrains
 294 its usefulness for evaluating pollution processes. In contrast, the EPICC-Model exhibits
 295 a more pronounced seasonal response. Its simulations during spring and summer are
 296 more consistent with CAMx, reflecting its accuracy under lower background



297 concentration conditions. During the autumn and winter pollution seasons, its
298 simulation trends align more closely with CMAQ, capturing pollution accumulation
299 processes more effectively. This ability to respond to seasonal variations allows the
300 EPICC-Model to strike a better balance between accurately simulating extreme
301 pollution events and sustaining strong overall annual performance.

302 Figure 2 presents the performance of the EPICC-Model, CAMx, and CMAQ in
303 simulating MDA8 O₃ concentrations, evaluated against observations from 1,644
304 national monitoring stations across China. Observational data reveal a typical
305 photochemically-driven seasonal pattern in O₃ concentrations: summer months exhibit
306 peak levels due to enhanced VOC-NO_x chain reactions under intense solar radiation
307 and elevated temperatures (Seinfeld and Pandis, 2016; Sillman, 1999), while winter and
308 spring maintain background concentrations resulting from reduced reaction activity
309 associated with decreased O₃ photolysis rates (J_{O_3}) and lower OH radical concentrations
310 (Wang et al., 2019). The time series analysis (Figure 2a) shows that all three models
311 reasonably reproduced the seasonal variation of O₃ concentrations, yet notable
312 differences emerged across concentration levels. The EPICC-Model performed
313 particularly well during high-concentration episodes, effectively capturing the peak
314 levels of O₃ pollution. In contrast, both CAMx and CMAQ, while capable of
315 reproducing high-concentration trends, systematically underestimated peak magnitudes
316 with maximum negative biases reaching -20 $\mu\text{g m}^{-3}$. This discrepancy mainly stems
317 from differences in chemical mechanisms design among the models. The EPICC-Model
318 incorporated heterogeneous HONO formation and nitrate photolysis pathways that
319 produce HONO, significantly enhanced the initial concentration of OH radicals. This
320 accelerated the oxidation of VOCs and promoted rapid O₃ formation, thereby
321 improving model performance during high-concentration periods (EPICC-Model
322 Working Group, 2025; Wang et al., 2025; Zhang et al., 2022). In addition, the EPICC-
323 Model employed the CB6r5 chemical mechanism, which offered more comprehensive
324 representation of BVOC oxidation (especially isoprene) compared to CB6r3 (used in
325 CMAQ) and CB05 (used in CAMx), thereby increasing O₃ formation potential
326 (Yarwood et al., 2020). Under low concentration background conditions, CMAQ
327 captured the general trend reasonably well but exhibited a systematic positive bias,
328 which may be attributed to its use of the ACM2 vertical mixing scheme that tends to
329 produce an overly deep boundary layer and enhanced NO₂ photolysis radical production
330 (Hu et al., 2010). The EPICC-Model showed the smallest absolute bias but with a
331 slightly weaker trend correlation.



332
333
334

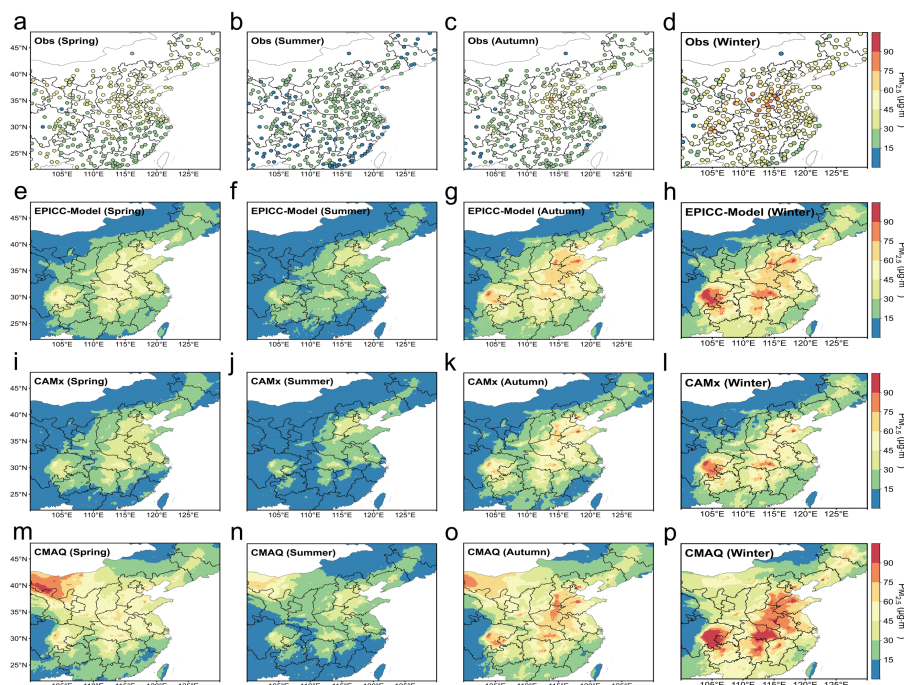
Figure 2. Comparison of simulated and observed daily MDA8 O₃ concentrations across China in 2021.

335
336
337
338
339
340
341
342
343
344
345
346

Statistical analysis indicates that CAMx exhibited the highest correlation coefficient ($R=0.94$) with well-controlled absolute bias despite its systematic underestimation. CMAQ showed a slight overestimation throughout the year but maintains a strong temporal correlation ($R=0.93$), demonstrating good capability in capturing temporal variations. Notably, the EPICC-Model not only accurately captured peak concentrations but also achieved the lowest annual NMB, reflecting a more robust performance overall. The scatter plot (Figure 2b) further corroborates these findings: all three models show excellent FAC2 values with well-clustered data points. CMAQ data points predominantly lie above the 1:1 reference line, indicating a tendency to overestimate; CAMx points mostly fall below the line, indicating underestimation; whereas the EPICC-Model achieves a better balance between overestimation and underestimation, delivered the best overall simulation performance.

347
348
349
350
351
352

Figure 3 compares the simulated spatial distributions of PM_{2.5} for the four seasons of 2021 produced by the EPICC-Model, CAMx, and CMAQ, revealing notable differences in regional simulation consistency and bias characteristics among the three models. As shown in Figure 3, the Index of Agreement (IOA) values vary across models and seasons, exhibiting clear seasonal patterns that quantitatively support the spatial distribution differences.



353

354 **Figure 3.** Seasonal spatial distributions of simulated PM_{2.5} concentrations, with spring (March-
355 May), summer (June-August), autumn (September-November), and winter (December-February).

356 **Table 3.** IOA for the spatial distribution of PM_{2.5} simulated by different models.

	Spring	Summer	Autumn	Winter	Year
EPIC-Model	0.63	0.62	0.60	0.81	0.80
CAMx	0.60	0.64	0.68	0.76	0.78
CMAQ	0.72	0.58	0.54	0.73	0.77

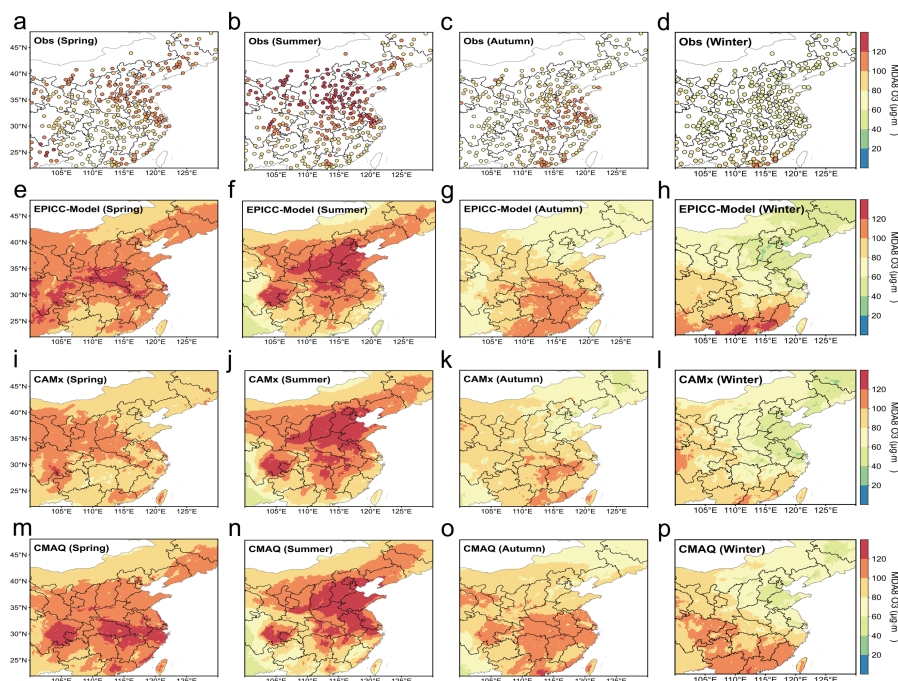
357 In spring, under the influence of northwesterly winds, dust transport combined
358 with local industrial emissions led to high PM_{2.5} concentrations mainly distributed over
359 North China, Northwest arid basins, and the Sichuan-Yunnan region. All three models
360 effectively reproduced the pollution pattern, with IOA values exceeding 0.60, and
361 CMAQ achieved the highest IOA of 0.72. Since dust concentrations were excluded
362 from the particulate matter assessment in this study, all three models consistently
363 underestimated PM_{2.5} levels in the arid Northwest and southwestern plateau regions. In
364 summer, influenced by the southeastern monsoon and intensive precipitation, PM_{2.5}
365 remain generally low across China with reduced regional variability. The three models
366 exhibited similar spatial consistency nationwide, with IOA values ranging between 0.58
367 and 0.64. However, in the high-humidity coastal regions of South China, the EPIC-
368 Model and CMAQ demonstrated slight advantages over CAMx in simulation accuracy.
369 In autumn, the nationwide PM_{2.5} concentrations rebounded due to an increase in
370 stagnant weather conditions and a reduced boundary layer height. All three models
371 showed varying degrees of overestimation in North China and the Sichuan Basin, likely
372 related to ACM2/YSU schemes underestimating mixing layer height and weakening



373 vertical diffusion at night (Jia et al., 2023). During this period, CAMx achieved the
374 highest IOA value of 0.68, the EPICCC-Model scores 0.60, while CMAQ dropped to its
375 annual minimum of 0.54. In winter, PM_{2.5} concentrations reached their annual peak
376 driven by low temperatures, temperature inversions, subsidence, and heating emissions.
377 All three models successfully reproduced the pollution patterns in polluted regions like
378 North and Central China. The EPICCC-Model demonstrated exceptional performance
379 with an IOA of 0.81, while CMAQ and CAMx maintained strong consistency at 0.73
380 and 0.76, respectively. However, all models unrealistically simulate higher PM_{2.5}
381 concentrations in the Sichuan Basin compared to Henan Province. This discrepancy
382 may have resulted from differences in emission estimates between the two regions:
383 anthropogenic emissions in the Sichuan Basin are likely overestimated in the models,
384 whereas frequent agricultural activities in Henan may lead to underestimation of NH₃
385 emissions, thereby suppressing nitrate aerosol formation. Previous studies have
386 demonstrated that spatial errors in NH₃ emissions significantly impact nitrate-driven
387 heavy pollution events (Kang et al., 2016; Kong et al., 2019; Liu et al., 2021).

388 Overall, all three models reliably simulate PM_{2.5} spatial distributions, with annual
389 mean IOA values above 0.77. The EPICCC-Model performs best (IOA=0.80), showing
390 highest consistency in winter and heavily polluted North China. CAMx shows
391 consistent performance (IOA=0.78) and is suitable for multi-seasonal averages but
392 underestimates high-humidity regions and responds weakly to severe pollution. CMAQ
393 shows slightly lower consistency (IOA=0.77), performs better in spring and winter,
394 declines in summer and autumn, and exhibits a general positive bias, particularly in
395 winter.

396 Figure 4 shows the seasonal spatial distribution of MDA8 O₃ in 2021 from the
397 three models. Given the strong seasonal variability of O₃, model performance was
398 quantitatively evaluated using the IOA metric, with detailed results provided in Table
399 4.



400

401 **Figure 4.** Seasonal spatial distributions of simulated MDA8 O₃ concentrations, with spring (March-
402 May), summer (June-August), autumn (September-November), and winter (December-February).

403 **Table 4.** IOA for the spatial distribution of MDA8 O₃ simulated by different models.

	Spring	Summer	Autumn	Winter	Year
EPICC-Model	0.56	0.79	0.74	0.77	0.85
CAMx	0.53	0.85	0.70	0.76	0.87
CMAQ	0.33	0.85	0.78	0.75	0.84

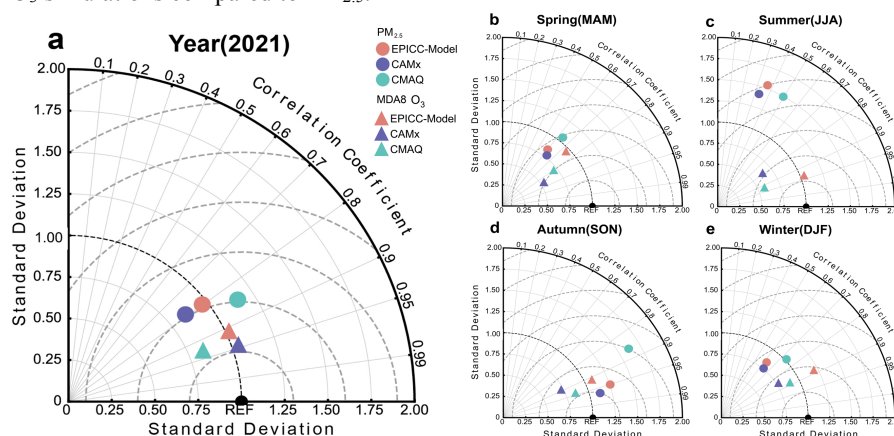
404 In spring, O₃ pollution exhibits a multi-centered and scattered distribution pattern.
405 The EPICC-Model reproduced this pattern well (IOA = 0.56) and outperforms CAMx
406 and CMAQ, particularly in the high-concentration areas like Yunnan. CAMx generally
407 underestimated O₃ nationwide, which may be associated with the use of the CB05
408 chemical mechanism and the 14 σ_p vertical configuration adopted in this study. (Ren et
409 al., 2022; Tang et al., 2011). CMAQ, in contrast, produced an unrealistic high-O₃ belt
410 over the Yangtze River plain with a much lower IOA of 0.33. In summer, a high O₃
411 concentration belt forms over the mid-latitudes (30° N ~40° N), and all three models
412 successfully reproduced the enhanced O₃ levels with the highest spatial consistency
413 observed throughout the year. The summer IOA values for the EPICC-Model, CAMx,
414 and CMAQ reach 0.79, 0.87, and 0.85, respectively. Given that all three models were
415 driven by meteorological fields derived from the same WRFv3 simulation, regional O₃
416 levels are primarily controlled by photochemical production rather than constrained by
417 boundary inputs (Li et al., 2019a). In autumn, national O₃ declines as solar radiation
418 weakens, with pollution centers shifting to eastern and southeastern coasts. All three
419 models performed similarly (IOA 0.70–0.74). CMAQ performed best in the Pearl River



420 Delta, accurately reproducing localized high concentrations, as supported by previous
 421 studies (Jiang et al., 2010; Wang et al., 2010). The EPIC-Model ranks second with
 422 slight overestimation in northern Jiangxi, and CAMx continues to underestimate O₃. In
 423 winter, due to extremely weak solar radiation, reduced stratosphere-troposphere
 424 exchange, high NO_x emissions, and limited boundary layer height, nationwide O₃
 425 concentrations drop to their annual minimum and shift southward. All models perform
 426 steadily (IOA 0.75–0.77). The EPIC-Model captured accumulation over the coastal
 427 areas of southern China but slightly overestimates, CAMx shifted high concentrations
 428 southwest, and CMAQ overestimated in northern regions while missing the southward
 429 O₃ shift.

430 Comprehensive evaluation indicates that the EPIC-Model shows consistent
 431 seasonal MDA8 O₃ performance with an annual IOA of 0.85, capturing O₃ distribution
 432 across China. CAMx has slightly higher consistency (IOA 0.87) but systematically
 433 underestimates in spring, autumn, and winter and misses localized peaks. CMAQ
 434 performs well in summer and autumn, especially over the Pearl River Delta, but IOA
 435 drops to 0.33 in spring and overestimates in winter, indicating a need to improve
 436 boundary layer and dry deposition schemes.

437 To comprehensively evaluate model performance, this study uses Taylor diagrams
 438 to compare the EPIC-Model, CAMx, and CMAQ simulations with observations on
 439 both annual and seasonal scales. The Taylor diagram simultaneously displays the
 440 correlation coefficient (R), normalized standard deviation (STD), and centered root
 441 mean square error (RMSE). In the diagram, the radial distance represents STD, the
 442 angular coordinate indicates R, and dashed contours denote RMSE relative to
 443 observations. The “REF” point (R = 1, STD = 1) represents perfect agreement with
 444 observations. The annual results (Figure 5a) show that all three models perform
 445 satisfactorily in simulating PM_{2.5} and MDA8 O₃, with particularly strong performance
 446 for MDA8 O₃. Correlation coefficients exceed 0.75 for all models, while RMSE and
 447 STD remain relatively low, indicating lower variability and higher accuracy in MDA8
 448 O₃ simulations compared to PM_{2.5}.



449
 450 **Figure 5.** Taylor diagrams of PM_{2.5} and MDA8 O₃ for the three models on annual and seasonal
 451 scales.



452 Seasonally, PM_{2.5} simulation accuracy exhibits marked variations: during winter
453 and spring high-concentration periods, all three models show comparable performance,
454 with CMAQ demonstrating greater ability to replicate pollution peaks (STD \approx 1, closest
455 to observations). Model performance declines significantly under summer's low-
456 background conditions (R<0.55, elevated RMSE/STD), indicating enhanced error
457 during high-concentration periods. Autumn sees performance recovery, with CAMx
458 achieving R=0.97. In contrast, MDA8 O₃ simulations show more robust seasonal
459 consistency: while spring remains the weakest season (R>0.7), the EPICCC-Model and
460 CMAQ maintain low errors. The EPICCC-Model excels during summer O₃ peaks (R \approx
461 0.95, lowest RMSE/STD), CMAQ leads in autumn, and all models converge in winter
462 (R=0.8-0.9), effectively capturing O₃ spatiotemporal patterns.

463 Overall, the EPICCC-Model demonstrates strong robustness in seasonal O₃
464 simulations, maintaining consistently low standard deviations and showing clear
465 advantages during the summer pollution peak. In contrast, CAMx and CMAQ exhibit
466 relative strengths in PM_{2.5} simulations: CAMx performs particularly well under the
467 complex meteorological conditions of autumn, while CMAQ better captures pollutant
468 accumulation processes during the stable boundary layer conditions in winter, reflecting
469 their respective adaptability.

470 **3.2 Evaluation of PM_{2.5} chemical composition simulations**

471 Based on the spatiotemporal variations of PM_{2.5} total concentrations simulated by
472 each model, the performance of the EPICCC-Model, CAMx, and CMAQ in simulating
473 major chemical components was further evaluated. Figure 6 presents the average
474 relative contributions and absolute concentrations of key PM_{2.5} components in ten
475 representative cities across urban clusters, including the Beijing-Tianjin-Hebei,
476 Yangtze River Delta, Chengdu-Chongqing, and the Middle Reaches of the Yangtze
477 River regions. Overall, all three models reasonably reproduced the observed chemical
478 composition structure characterized by a predominance of nitrate (NO₃⁻), which is
479 consistent with previous findings (Huang et al., 2021). Observations indicated that
480 NO₃⁻ accounted for approximately 31.2% to 42.4% of PM_{2.5} mass in most cities. This
481 dominant feature was reproduced by all models, although the simulated concentrations
482 tended to be overestimated to varying degrees.

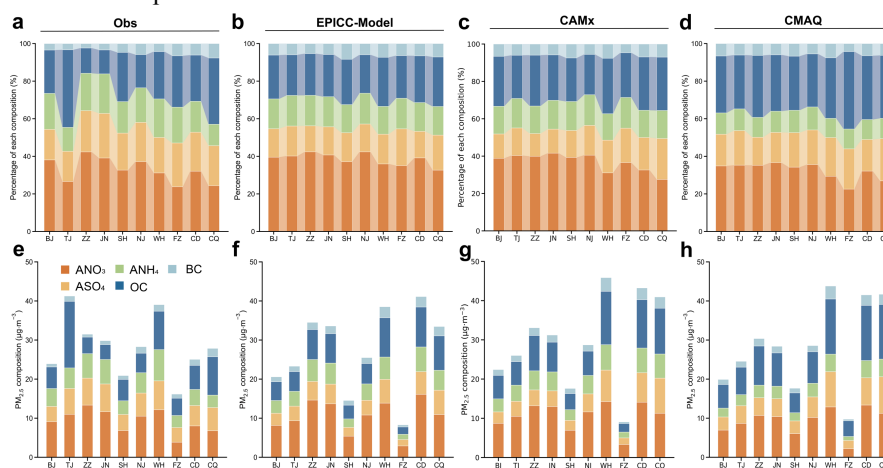
483 Meanwhile, all three models consistently underestimated sulfate (SO₄²⁻), a bias
484 consistent with existing research findings (Shao et al., 2019), which may stem from
485 underestimating SO₂ oxidation rates or uncertainties in intra-cloud aqueous-phase
486 chemical mechanisms. The insufficient formation of SO₄²⁻ not only limits the
487 production of ammonium sulphate [(NH₄)₂SO₄] but also reduces the consumption
488 potential of NH₃ (Gao et al., 2018), thereby suppressing the simulated concentration of
489 ammonium (NH₄⁺). In addition, the reduced formation of ammonium sulfate may leave
490 more free NH₃ available to react with HNO₃, potentially enhancing the formation of
491 ammonium nitrate (NH₄NO₃) and contributing to the overestimation of nitrate in some
492 regions.

493 For OC, although certain deviations are observed in individual cities, the overall
494 simulation performance of the three models remains within an acceptable range (Miao



495 et al., 2020). Among them, the EPIC-Model and CAMx produced results that are
 496 closer to observations, while CMAQ tends to systematically overestimate OC
 497 concentrations. This systematic bias may stem from the introduction of Potential
 498 Combustion SOA (PCSOA) species starting from CMAQv5.2. PCSOA serves as a
 499 surrogate secondary organic aerosol species to compensate for the lack of combustion-
 500 related SVOC and IVOC emissions in current inventories. However, the model
 501 estimates PCSOA concentrations through parameterized precursor emissions and
 502 simplified processes including OH oxidation and gas-particle partitioning. The
 503 associated uncertainties may result in regional and temporal discrepancies, failing to
 504 reflect the real-world variations in PCSOA and consequently leading to simulation
 505 biases (Murphy et al., 2017; Pennington et al., 2021). Overall, all three models share
 506 substantial uncertainties in SOA-related mechanisms, representing a common
 507 limitation.

508 Black carbon (BC) is the least abundant component of PM_{2.5}, with observed
 509 concentrations ranging from 0.7 to 2.1 μg m⁻³. All models exhibit generally consistent
 510 performance in simulating its relative contribution, with slight overestimations
 511 observed in Beijing, Tianjin, and Zhengzhou. These biases are primarily attributed to
 512 uncertainties in BC emission inventories, particularly from biomass burning and motor
 513 vehicle sources (Hong et al., 2017). Due to its low chemical reactivity in the atmosphere
 514 and limited removal through secondary processes, BC simulations are highly sensitive
 515 to emission inputs.

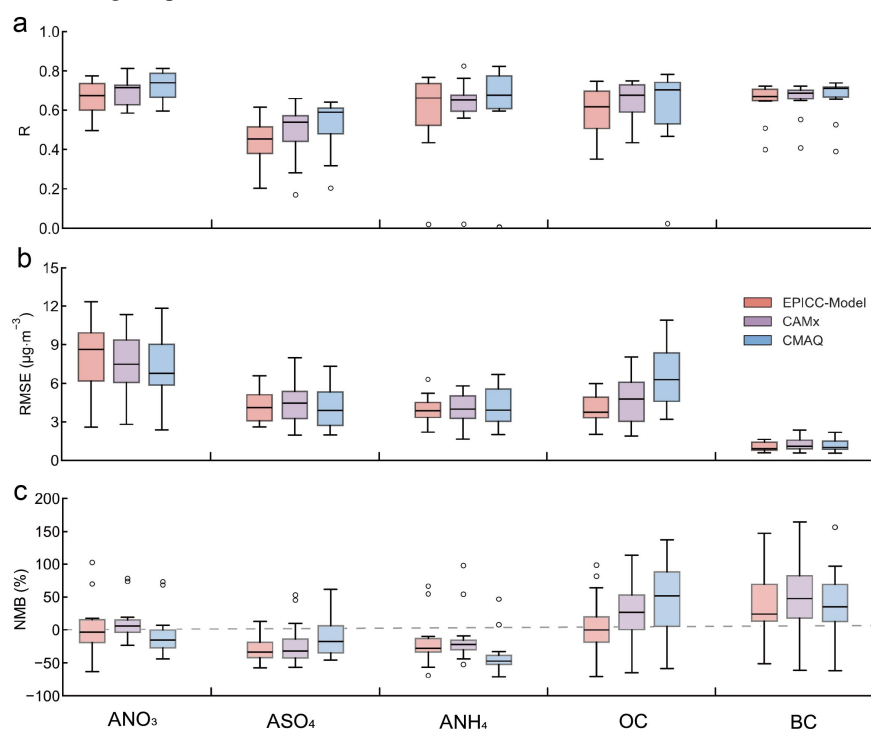


516
 517 **Figure 6.** Comparison of simulated and observed aerosol components in representative Chinese
 518 cities. ASO₄, ANO₃, ANH₄, OC, and BC denote sulfate, nitrate, ammonium, organic carbon, and
 519 black carbon in PM_{2.5}, respectively. The locations of monitoring sites are as follows: BJ (Beijing;
 520 116.41° E, 40.04° N), TJ (Tianjin; 117.21° E, 39.17° N), ZZ (Zhengzhou; 113.73° E, 34.77° N), JN
 521 (Jinan; 117.06° E, 36.66° N), SH (Shanghai; 121.53° E, 31.23° N), NJ (Nanjing; 118.76° E, 32.07°
 522 N), WH (Wuhan; 114.37° E, 30.54° N), FZ (Fuzhou; 119.31° E, 26.10° N), CD (Chengdu; 104.09°
 523 E, 30.64° N), and CQ (Chongqing; 106.47° E, 29.62° N).

524 As shown in the stacked bar charts of PM_{2.5} absolute concentrations in Figure 6e-
 525 7h, Tianjin exhibits the highest levels among the selected cities, followed by Wuhan,



526 while Fuzhou shows the lowest. This spatial pattern is closely related to regional
 527 emission intensity and meteorological conditions. The three models reasonably
 528 reproduce these concentrations in most cities, particularly in Nanjing. However,
 529 systematic biases exist in certain locations. Simulated concentrations in Tianjin are
 530 substantially lower than observations, primarily due to underestimation of OC
 531 associated with uncertainties in SOA formation mechanisms. In contrast,
 532 concentrations in Chengdu and Chongqing are consistently overestimated across all
 533 models, indicating an amplified model response to pollution episodes in central China.
 534 Overall, while the models capture the major chemical composition features, their ability
 535 to accurately reproduce absolute concentrations and regional variability remains limited,
 536 highlighting the need for refined emission inventories and improved representation of
 537 meteorological processes.



538
 539 **Figure 7.** Performance metrics of aerosol component simulations across models in representative
 540 Chinese cities.

541 Figure 7 presents boxplots of statistical evaluation metrics (R, RMSE, and NMB)
 542 based on ten representative cities to quantify the simulation accuracy and systematic
 543 biases of each model. Regarding the overall distribution of R values, a clear “stepwise”
 544 difference is observed among the three models. CMAQ generally exhibits higher R
 545 values across PM_{2.5} components than the EPIC-Model and CAMx, indicating stronger
 546 capability in reproducing spatiotemporal variability. Among individual components,
 547 NO₃⁻ shows the highest correlation (median R > 0.6) with no outliers, suggesting robust
 548 representation. NH₄⁺ and OC display slightly lower R values, reflecting moderate



549 uncertainty but acceptable overall performance. SO_4^{2-} shows dispersed correlations and
550 some low R values, indicating substantial simulation errors, likely due to insufficient
551 representation of regional secondary aerosol formation. BC exhibits the most compact
552 R distribution, with low inter-city variability, reflecting robust and consistent
553 simulation by all models. The RMSE analysis shows larger errors for NO_3^- and OC,
554 with some cities reaching $12 \mu\text{g m}^{-3}$ and median values above $6 \mu\text{g m}^{-3}$, reflecting
555 sensitivity to meteorology, secondary processes, and SOA-related uncertainties. The
556 EPIC-Model performs well in this aspect. SO_4^{2-} and NH_4^+ exhibit moderate RMSE,
557 indicating relatively low variability simulations, while BC shows the lowest RMSE and
558 most compact distribution, suggesting high accuracy. The NMB results show that the
559 deviations of NO_3^- , SO_4^{2-} , and NH_4^+ are relatively constrained, although
560 overestimations or underestimations still occur in some cities. In contrast, the NMB
561 boxplots for OC and BC exhibit significant elongation, with deviations ranging from -
562 50% to +150% in certain locations. The high bias of OC is mainly attributed to
563 inaccuracies in the representation of SOA formation and precursor emissions, while the
564 large relative deviations of BC are likely due to its low ambient concentrations, where
565 even minor absolute errors can lead to amplified relative discrepancies.

566 A cross-model comparison reveals that CMAQ exhibits the highest correlation
567 coefficients, particularly excelling in reproducing the spatial and temporal patterns of
568 NO_3^- and NH_4^+ . However, it shows a tendency to overestimate OC concentrations.
569 CAMx shows intermediate performance across most components. While the EPIC-
570 Model demonstrates relatively lower consistency in species simulation, maintains more
571 stable performance in terms of RMSE and NMB.

572 3.3 AQI and pollution forecast accuracy

573 To comprehensively evaluate the applicability of the three CTMs in graded air
574 quality forecasting, this study systematically assesses the performance of the EPIC-
575 Model, CAMx, and CMAQ in the Air Quality Index (AQI) level prediction based on
576 the *Technical guideline for numerical forecasting of ambient air quality* (HJ1130-2020).
577 According to the evaluation criteria defined in the *Technical Regulation for the*
578 *Assessment of Urban Ambient Air Quality Index (AQI) Forecasting (Trial)* (China
579 National Environmental Monitoring Center, 2020), and considering the needs of
580 operational forecasting, a prediction is deemed accurate if the observed AQI falls within
581 $\pm 25\%$ of the forecasted value. It should be noted that, as dust events were not included
582 in the simulations, the “heavy pollution” and “severe pollution” categories were
583 combined in the subsequent analysis. Based on this criterion, all three models exhibit a
584 consistent pattern across different pollutants and pollution levels: the higher the
585 pollution level, the lower the forecasting accuracy. The algorithms and definitions of
586 AQI and IAQI are provided in the Supplementary Material for reference.

587 In terms of overall forecasting accuracy, CAMx performs best in predicting AQI
588 (84%), $\text{PM}_{2.5}$ (81%), and MDA8 O_3 (89%) levels. The EPIC-Model shows reliable
589 performance in forecasting good to moderate pollution levels, indicating strong
590 capability in simulating the initial formation and accumulation of secondary pollutants
591 under relatively low to moderate precursor concentrations. This is largely due to the



592 EPICC-Model’s incorporation of key heterogeneous reaction mechanisms that critically
 593 influence the rapid growth of secondary inorganic aerosols during heavy pollution
 594 episodes (EPICC-Model Working Group, 2025), including SO₂ manganese-catalyzed
 595 oxidation (Wang et al., 2021), N₂O₅ heterogeneous hydrolysis (Yang et al., 2024), and
 596 HONO heterogeneous formation (Zhang et al., 2022). CMAQ demonstrates superior
 597 performance in identifying moderate and higher pollution levels, particularly exhibiting
 598 notably higher accuracy than CAMx and the EPICC-Model for moderate to heavy and
 599 severe PM_{2.5} levels. However, all three models show generally low accuracy under
 600 extreme pollution scenarios, highlighting limitations in current chemical transport
 601 models for simulating nonlinear pollution buildup and the synergistic effects of extreme
 602 weather and pollution.

603 **Table 5.** Comparison of AQI level forecast accuracy for 337 Chinese cities.

Model	Excellent	Good	Light Pollution	Moderate Pollution	Heavy and Severe Pollution	Accuracy
EPICC-Model	85%	85%	62%	39%	23%	82%
CAMx	90%	87%	57%	31%	11%	84%
CMAQ	83%	88%	63%	41%	36%	82%

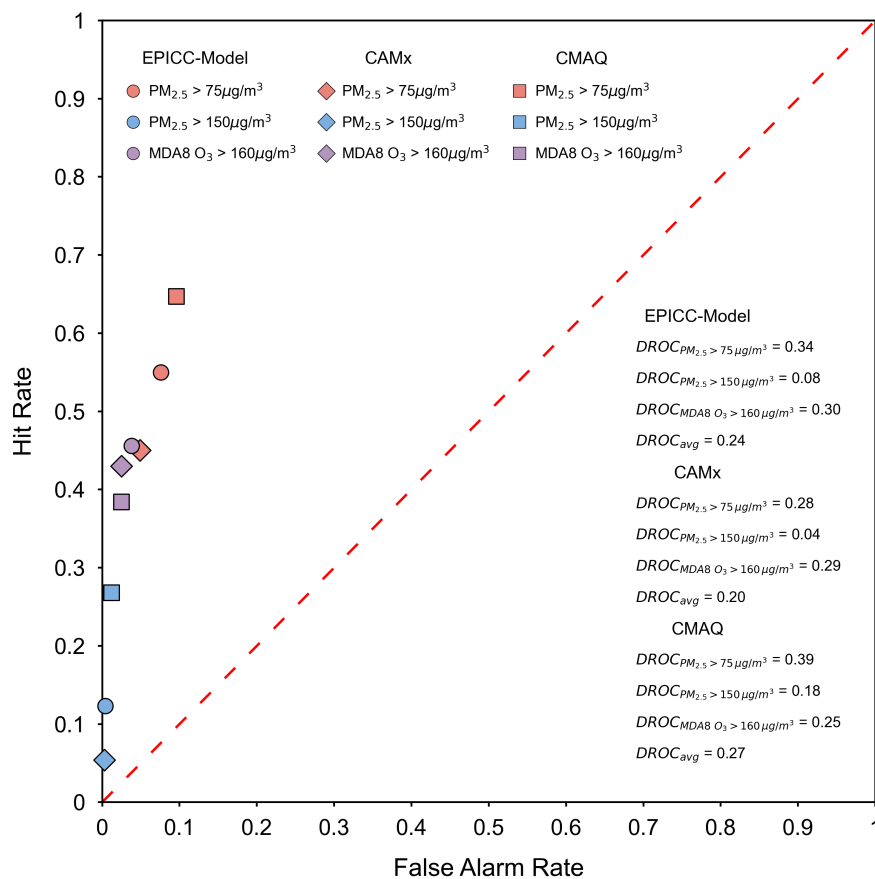
604 **Table 6.** Comparison of PM_{2.5} IAQI level forecast accuracy at 1,644 monitoring sites in China with
 605 observations.

Model	Excellent	Good	Light Pollution	Moderate Pollution	Heavy and Severe Pollution	Accuracy
EPICC-Model	85%	69%	51%	35%	25%	79%
CAMx	90%	68%	46%	26%	11%	81%
CMAQ	83%	68%	50%	40%	41%	77%

606 **Table 7.** Comparison of MDA8 O₃ IAQI level forecast accuracy at 1,644 monitoring sites in China
 607 with observations.

Model	Excellent	Good	Light Pollution	Moderate Pollution	Heavy and Severe Pollution	Accuracy
EPICC-Model	91%	84%	57%	23%	6%	87%
CAMx	96%	84%	56%	23%	12%	89%
CMAQ	85%	92%	60%	14%	6%	86%

608 Given the high sensitivity and risk posed by polluted weather and severe pollution
 609 events to public health and environmental management, this study further focuses on
 610 the forecasting performance of PM_{2.5} and MDA8 O₃ pollution events. Based on metrics
 611 such as hit rate, false alarm rate, and the distance from the random operating
 612 characteristic (DROC) (definitions and calculation methods are provided in the
 613 Supplementary Material), the forecast effectiveness for general pollution conditions
 614 (PM_{2.5} > 75 µg m⁻³ and MDA8 O₃ > 160 µg m⁻³) and severe pollution conditions (PM_{2.5} >
 615 150 µg m⁻³) is thoroughly analyzed to elucidate the applicability and potential
 616 limitations of each model under extreme pollution scenarios.



617

618 **Figure 8.** Comparison of CTMs performance based on hit rate and false alarm rate. Scatter points
 619 represent the performance of three models (EPICC-Model: circles, CAMx: diamonds, CMAQ:
 620 squares) under different pollution event thresholds: $PM_{2.5} > 75 \mu g m^{-3}$, $PM_{2.5} > 150 \mu g m^{-3}$, and
 621 $MDA8 O_3 > 160 \mu g m^{-3}$. The red dashed line indicates the random forecast reference line. The
 622 DROC metric, which quantifies model skill, is provided in the lower-right corner, with higher values
 623 indicating better model performance.

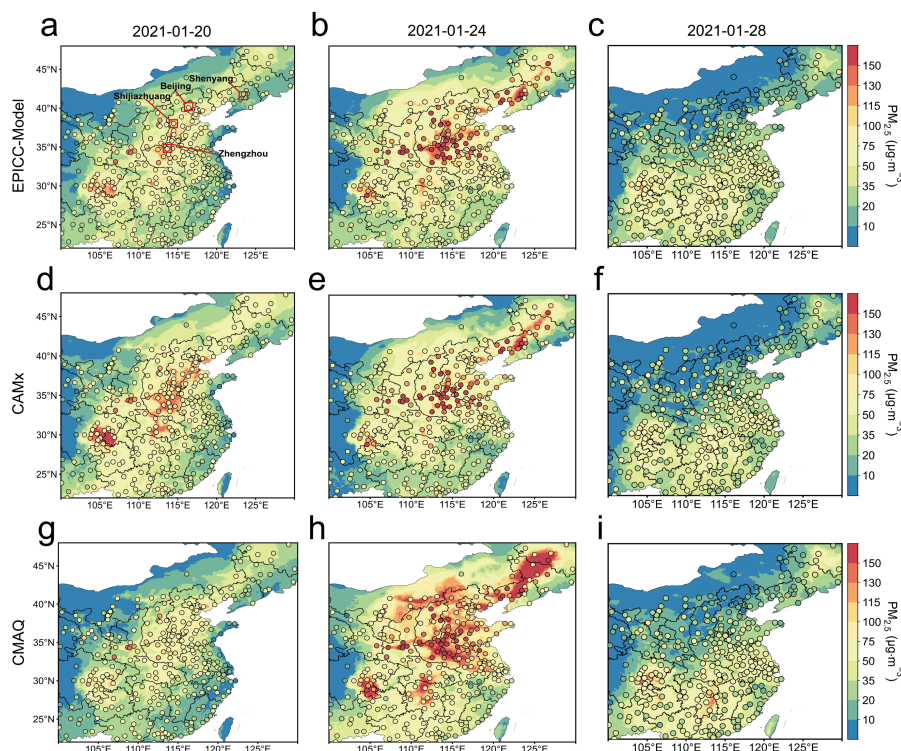
624 Figure 8 visually compares the forecast performance of three models under
 625 different pollution thresholds using scatter points in ROC space. For general pollution
 626 scenarios ($PM_{2.5} > 75 \mu g m^{-3}$), CMAQ shows the highest hit rate (64.7%) but is
 627 accompanied by a relatively high false alarm rate (9.6%), indicating a tendency toward
 628 systematic overestimation. CAMx achieves the lowest false alarm rate (4.9%), likely
 629 because it tends to underpredict $PM_{2.5}$ levels and forecast fewer high pollution events.
 630 However, its hit rate is also relatively low (45.0%), reflecting a more conservative
 631 forecasting tendency. The EPICC-Model strikes a balance between hit rate (55.0%) and
 632 false alarm rate (7.6%), suggesting a trade-off between detection capability and false
 633 alarm occurrence. Under the more severe pollution condition ($PM_{2.5} > 150 \mu g m^{-3}$), the
 634 hit rates of all models decrease significantly. While CMAQ still maintains the highest



635 hit rate (26.8%), its miss rate reaches 73.2%. The EPICC-Model and CAMx show hit
 636 rates of only 12.3% and 5.4%, respectively, indicating limited responsiveness of current
 637 models to extreme pollution events. Nevertheless, all models maintain false alarm rates
 638 below 2%. This reflects limitations of the models in simulating extreme pollution
 639 conditions. For O₃ pollution events (MDA8 O₃ > 160 μg m⁻³), the EPICC-Model
 640 achieves the highest hit rate (45.6%), slightly higher than CAMx (43.0%) and CMAQ
 641 (38.4%), while also maintaining a low false alarm rate (3.8%). The DROC values
 642 provided in the lower-right table quantitatively reflect the above observations: CMAQ
 643 has the highest DROC (0.39) for general PM_{2.5} pollution events, while the EPICC-
 644 Model performs best for O₃ events (DROC=0.30). CAMx exhibits relatively low
 645 DROC across all thresholds.

646 3.4 Capability in capturing regional persistent pollution events

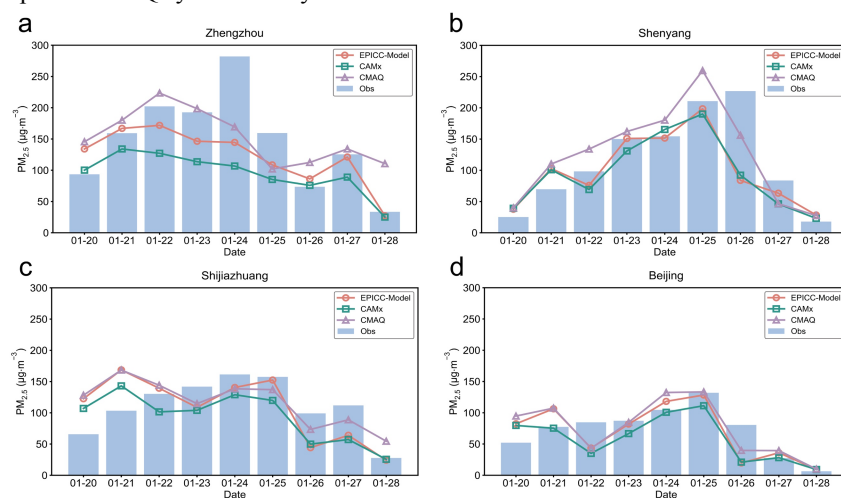
647 To further evaluate the capability of the EPICC-Model, CAMx, and CMAQ in
 648 simulating trans-regional and long-duration pollution episodes, this study selects
 649 typical persistent PM_{2.5} and O₃ events in 2021, and conducts a dedicated analysis
 650 incorporating pollutant transport pathways and the spatiotemporal consistency of
 651 meteorological fields.



652
 653 **Figure 9.** Spatiotemporal distribution of the persistent PM_{2.5} pollution event. Dots represent
 654 observed concentrations in 377 cities.



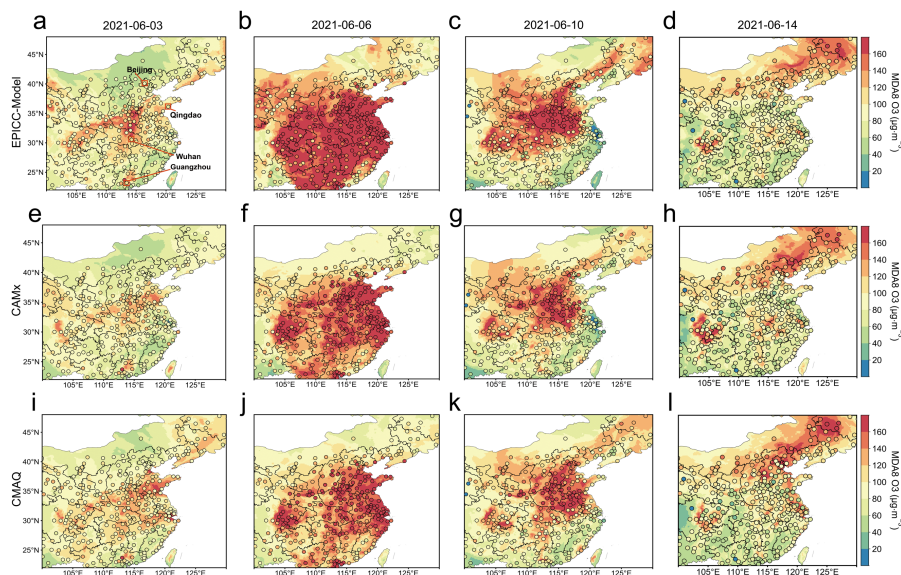
655 As shown in Figure 9, a persistent PM_{2.5} pollution event occurred in eastern and
 656 central China from January 20 to 28, 2021. Initially, pollution was concentrated
 657 between 30° N and 40° N, forming a “dual-core” pattern over the North China Plain
 658 and the Sichuan Basin. By January 24, PM_{2.5} concentrations peaked, with the pollution
 659 belt extending southeastward to the middle and lower Yangtze River regions and
 660 northeastward to the Songnen Plain. On January 28, under cold air influence,
 661 concentrations dropped below 75 μg m⁻³ in most areas, leaving only isolated hotspots.
 662 All three models captured the temporal evolution from initiation to dissipation. The
 663 EPICCC-Model showed better performance in reproducing spatial gradients and
 664 temporal patterns, particularly in the centre of the North China Plain and Yangtze River
 665 Middle-Reach corridor. CAMx reproduced the northeastward transport path but
 666 underestimated pollution intensity, failing to capture the strong core in Henan during
 the peak. CMAQ systematically overestimated concentrations.



668

669 **Figure 10.** Time series of PM_{2.5} concentrations in key cities along the pollution belt.

670 As shown in Figure 10, Zhengzhou recorded the first PM_{2.5} peak (>150 μg m⁻³) on
 671 January 21, with the pollution plume spreading northeastward and causing a delayed
 672 concentration rise in Shenyang. All four cities (Zhengzhou, Shenyang, Shijiazhuang,
 673 and Beijing) reached their maxima, though peak timings varied. During the clearing
 674 phase, driven by southward cold air intrusion, concentrations declined across all cities,
 675 with faster removal in Zhengzhou and Shijiazhuang than in Shenyang and Beijing. All
 676 three models reproduced the overall process but showed systematic timing biases, with
 677 peaks in Shenyang and Zhengzhou simulated 24-48 hours earlier than observed. Such
 678 deviations may result from inaccuracies in the simulated wind field evolution within
 679 the meteorological models. In terms of magnitude, CAMx underestimated and CMAQ
 680 overestimated concentrations in Zhengzhou, while the EPICCC-Model produced
 681 comparatively robust results. In the other three cities, all models tracked concentrations
 682 similarly.

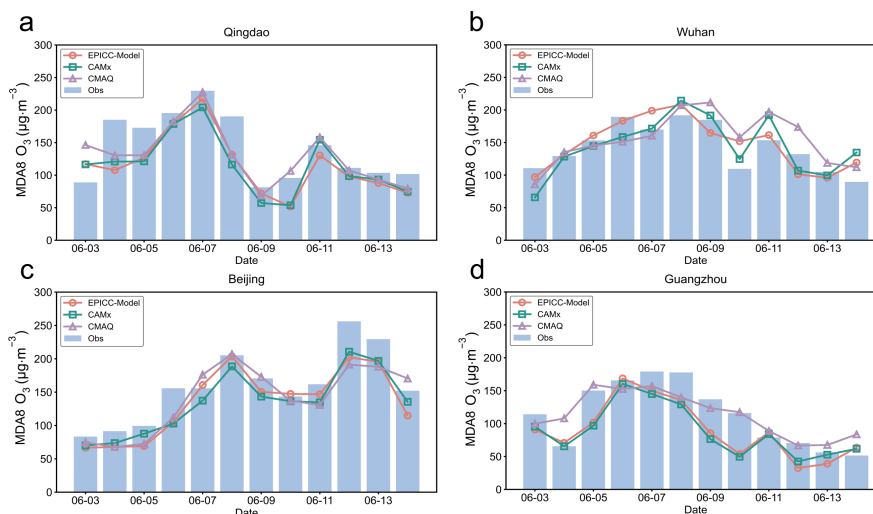


683

684 **Figure 11.** Spatiotemporal distribution of the persistent O₃ pollution event.

685 As shown in Figure 11, a persistent O₃ pollution episode occurred in China from
 686 June 3 to 14, 2021. The event began on June 3 with scattered pollution over the North
 687 China Plain and parts of Guangdong Province. By the peak stage on June 6, pollution
 688 intensity increased significantly, spreading to central, southeastern, and southern
 689 regions. By June 10, the pollution weakened and became more localized in North China
 690 and its western areas, while southern regions began clearing. By June 14, MDA8 O₃
 691 concentrations dropped below 100 µg m⁻³ across most areas, leaving only a few
 692 localized hotspots in Northeast China and Inner Mongolia. Elevated temperatures,
 693 strong solar radiation, and stagnant atmospheric conditions favored O₃ formation,
 694 whereas cold air intrusions promoted dispersion and removal.

695 During this persistent pollution event, all three models captured the full process of
 696 occurrence, development, and removal. Among them, the EPIC-Model best
 697 reproduced the spatial progression from central China to southeastern and southern
 698 regions and subsequent clearing toward the North China Plain and northeastern areas,
 699 although local overestimation occurred during the peak phase in the southeastern region,
 700 likely due to an excessively strong aerosol-radiation feedback. CAMx and CMAQ
 701 tended to underestimate pollution intensity in high-concentration areas, particularly
 702 during the peak on June 6 and the initial clearing stage on June 10, and did not fully
 703 reproduce the strong pollution exceeding 160 µg m⁻³ across Henan Province. In lower
 704 ozone areas, especially in central China, their predictions were generally consistent with
 705 the observed values, while the EPIC-Model slightly overpredicted ozone in some of
 706 these regions. Overall, the EPIC-Model outperformed the other two models in
 707 capturing spatiotemporal patterns, while CAMx and CMAQ showed deficiencies in
 708 reproducing peak concentrations.



709

710 **Figure 12.** Time series of O₃ concentrations in key cities along the pollution belt.

711 The pollution event occurred over central and eastern China between 30° N and
 712 40° N. Qingdao first entered O₃ pollution on June 4, with MDA8 O₃ exceeding 160 µg
 713 m⁻³. The pollution then maintained high concentrations and expanded northward and
 714 southward, reaching Qingdao, Wuhan, Beijing, and Guangzhou by June 6. After June
 715 9, the first clearing phase began from south to north, with Guangzhou improving first,
 716 followed by Wuhan and Qingdao, while the pollution center shifted to the North China
 717 Plain and northeastern regions, causing a sharp rise in Beijing around June 12. By June
 718 14, most regions had cleared, with Beijing showing the fastest decline, likely due to
 719 enhanced cold air activity and higher boundary layer. All three models captured the full
 720 progression in Beijing and Qingdao accurately. For Wuhan and Guangzhou, where peak
 721 concentrations persisted, model predictions showed approximately one-day deviations,
 722 likely due to limited responses to abrupt meteorological changes.

723 **4 Conclusions**

724 This study presents a systematic evaluation of three CTMs (EPIC-Model, CAMx,
 725 and CMAQ) for PM_{2.5} and MDA8 O₃ simulations over China in 2021, using unified
 726 WRF meteorological fields and multi-source emission inventories. The work fills a
 727 critical research gap by providing the first comprehensive comparison of the EPIC-
 728 Model against established CTMs. The results indicate that all three models can
 729 effectively reproduce the spatiotemporal evolution characteristics of PM_{2.5} and MDA8
 730 O₃ (PM_{2.5}: R = 0.79-0.85, MDA8 O₃: R = 0.91-0.94). In PM_{2.5} simulations, the EPIC-
 731 Model shows seasonal turning points, with spring and summer results tending toward
 732 the underestimation trend of CAMx, while autumn and winter results align more closely
 733 with the overestimation tendency of CMAQ. Spatially, it exhibits higher consistency
 734 (annual IOA = 0.80), particularly in winter and over heavily polluted North China,
 735 effectively capturing pollution patterns and peaks. For O₃, the EPIC-Model performs



736 well during high-concentration summer episodes, accurately reproducing extremes,
737 thanks to enhanced heterogeneous HONO formation and nitrate photolysis, which
738 increase OH radicals and accelerate VOC oxidation, and the CB6r5 chemical
739 mechanism that better represents biogenic VOC oxidation. Furthermore, the EPICC-
740 Model produces particularly accurate O₃ simulations over the eastern, central, and
741 Chengdu-Chongqing regions. Notably, all three models share common deficiencies in
742 PM_{2.5} simulations. Systematic underestimations occur in arid northwestern China due
743 to unaccounted dust processes, highlighting the critical influence of natural emissions
744 on model accuracy. Conversely, autumn-winter overestimations prevail in North China
745 and the Sichuan Basin, attributable to the ACM2/YSU boundary layer schemes
746 underestimating mixing layer height and weakening nocturnal vertical diffusion,
747 thereby inadequately reproducing inversion layers and pollution accumulation.
748 Uncertainties in emission inventories further exacerbate regional biases, such as
749 potential overestimation of anthropogenic emissions in the Sichuan Basin and
750 underestimation of agricultural NH₃ emissions in Henan, which affects nitrate aerosol
751 formation. Future improvements should incorporate dust processes, refine boundary
752 layer parameterizations to better simulate pollutant accumulation under stable
753 meteorological conditions, and employ higher-resolution emission inventories with
754 improved temporal variability characterization.

755 In terms of PM_{2.5} component simulations, the EPICC-Model, CAMx, and CMAQ
756 all reasonably reproduce the chemical composition characterized by NO₃⁻ dominance
757 and associated regional variations. Compared with CAMx and CMAQ, the EPICC-
758 Model exhibits smaller biases in SO₄²⁻ and NH₄⁺, with more robust control of absolute
759 concentrations as reflected in RMSE and NMB, indicating a relatively consistent
760 overall performance, although its correlation metrics are slightly lower than the other
761 two models. Nevertheless, all three models share common limitations: SO₄²⁻ is
762 generally underestimated, leading to insufficient formation of (NH₄)₂SO₄ and lower
763 NH₄⁺ concentrations; SOA formation remains highly uncertain, influenced by precursor
764 VOC emissions, oxidation pathways, and gas-particle partitioning parameterizations,
765 resulting in spatial deviations in OC; BC simulations are highly sensitive to emission
766 inventories, occasionally leading to slight overestimations in certain cities. Addressing
767 these issues in future work should focus on optimizing secondary inorganic aerosol
768 chemistry, improving SOA formation mechanisms and precursor emissions, and
769 enhancing the resolution and accuracy of emission inventories to improve the models'
770 capability in reproducing PM_{2.5} chemical composition.

771 Regarding AQI level classification ability, CAMx achieved the highest overall
772 accuracy (84%), demonstrating particular strengths in distinguishing “excellent” and
773 “good” air quality levels. CMAQ is relatively accurate in pollution level identification,
774 with the highest hit rate (64.7%) in identifying general pollution where PM_{2.5} > 75 μg
775 m⁻³, but it has a high false alarm rate (9.6%), indicating a tendency toward over-
776 forecasting. The EPICC-Model shows higher hit rates in identifying PM_{2.5} light to
777 moderate pollution levels and MDA8 O₃ general pollution, achieving 45.6% for MDA8
778 O₃ > 160 μg m⁻³, compared with 43.0% for CAMx and 38.4% for CMAQ. The forecast
779 accuracy of all three models for single extreme pollution events was less than 2%,



780 indicating that the response capability of existing models to sudden pollution events
781 still needs further improvement. In addition, the EPICC-Model demonstrated relatively
782 balanced false alarm rates across all pollution types, suggesting a simulation capability
783 comparable to other mainstream models and particular effectiveness in capturing light
784 to moderate pollution and O₃ pollution.

785 In the simulation analysis of typical persistent PM_{2.5} and O₃ pollution events in
786 2021, the EPICC-Model demonstrated strong capabilities, particularly outperforming
787 CAMx and CMAQ in reproducing spatial distributions and pollution evolution. The
788 EPICC-Model successfully captured the entire process of pollution occurrence,
789 development, and clearance, particularly in the core area of the North China Plain and
790 the diffusion zone of the middle Yangtze River, where the simulation results were in
791 close agreement with observational data. CAMx and CMAQ, however, performed less
792 effectively in capturing persistent pollution events, both exhibiting significant
793 deviations during the simulation of severe pollution phases. CAMx underestimated
794 pollution intensity during severe pollution events, while CMAQ responded too rapidly
795 during the dissipation phase, leading to premature pollution decay (the average duration
796 of the pollution process was underestimated by 12-18 hours).

797 This study establishes a multi-model evaluation framework to systematically
798 compare the applicability and robustness of the EPICC-Model against internationally
799 established models over China. By identifying both model-specific limitations and
800 common challenges shared across different models, this work provides a clear pathway
801 for improving the next generation of atmospheric CTMs. The results not only offer
802 critical scientific support for air pollution control and policy-making in China, but also
803 serve as a valuable reference for other developing countries facing similar
804 environmental challenges. This study contributes to promoting the collaborative
805 development of global air quality modeling techniques and advancing sustainable
806 environmental governance.

807 **Code and data availability**

808 All models used in this study are open source and publicly available. The EPICC-
809 Model v1.0 source code is archived at <https://doi.org/10.5281/zenodo.20303367>.
810 CAMx v7.00 can be downloaded from <https://www.camx.com/download/source/>
811 (Ramboll, 2020), while CMAQ v5.3.3 is available through
812 <https://doi.org/10.5281/zenodo.5213949>. Meteorological fields were generated using
813 the WRF v3.9.1 (Skamarock et al., 2008), which is available from
814 https://www2.mmm.ucar.edu/wrf/users/download/get_source.html. Initial and
815 boundary conditions were derived from the NCEP FNL reanalysis dataset (NCEP,
816 2000), archived at <https://doi.org/10.5065/D6M043C6>. Anthropogenic emissions over
817 China were obtained from the MEIC inventory developed by Tsinghua University
818 (Geng et al., 2024), available at http://meicmodel.org.cn/?page_id=541&lang=en.
819 Chinese NH₃ emissions were taken from the PKU-NH₃ inventory, while biomass-
820 burning emissions were obtained from the China Open Biomass Burning Emissions
821 Inventory (Huang et al., 2012a, 2012b; Song et al., 2009; Kang et al., 2016). Both
822 datasets are available through the MEIC data platform at



823 http://meicmodel.org.cn/?page_id=1772&lang=en. Emissions outside China were
824 represented using the EDGAR v5.0 inventory (Crippa et al., 2020), available at
825 https://edgar.jrc.ec.europa.eu/dataset_ap50. Biogenic emissions were calculated online
826 using MEGAN v3.2, whose source code is archived at
827 <https://zenodo.org/records/10526206> (Guenther et al., 2012). Air quality observations
828 were obtained from the China National Environmental Monitoring Centre (CNEMC;
829 <https://www.cnemc.cn/>). The primary datasets generated and analysed in this study, as
830 well as the emission data employed (using the 15th of each month as an example), are
831 available in Zenodo at <https://doi.org/10.5281/zenodo.20843312>. Additional
832 supporting materials are available from the corresponding author upon reasonable
833 request.

834 **Author contributions**

835 ML, QW, WengdW, and HC conceptualized and organized the study. ML
836 performed the data analysis and drafted the manuscript. ML and XF conducted the
837 numerical simulations, and FY optimized the simulation code. XF and WeiW provided
838 data support. DL contributed to the meteorological model evaluation. ML, QW,
839 WengdW, and HC validated and analyzed the simulation results. KC, JZ, and ZW
840 reviewed the research findings and provided key feedback. All authors read and
841 approved the final manuscript.

842 **Competing interests**

843 The authors declare no competing interests.

844 **Acknowledgements**

845 We appreciate the technical support provided by the National Large Scientific and
846 Technological Infrastructure, the “Earth System Numerical Simulation Facility”
847 (<https://cstr.cn/31134.02.EL>).

848 **Financial support**

849 This study was supported by the National Key Research and Development Program
850 of China (Grant No. 2023YFC3705705 and 2024YFC3713603) and the Strategic
851 Priority Research Program of the Chinese Academy of Sciences (Grant No.
852 XDB0760400).

853 **Reference**

- 854 Amnuaylojaroen, T., Barth, M. C., Emmons, L. K., Carmichael, G. R., Kreasuwun, J.,
855 Prasitwattanaseree, S., and Chantara, S.: Effect of different emission inventories on modeled
856 ozone and carbon monoxide in Southeast Asia, *Atmos Chem Phys*, 2014.
- 857 Barnard, J. C., Chapman, E. G., Fast, J. D., Schmelzer, J. R., Slusser, J. R., and Shetter, R. E.: An
858 evaluation of the FAST-J photolysis algorithm for predicting nitrogen dioxide photolysis rates
859 under clear and cloudy sky conditions, *Atmos. Environ.*, 38, 3393–3403,
860 <https://doi.org/10.1016/j.atmosenv.2004.03.034>, 2004.
- 861 Bessagnet, B., Pirovano, G., Mircea, M., Cuvelier, C., Aulinger, A., Calori, G., Ciarelli, G., Manders,



- 862 A., Stern, R., Tsyro, S., García Vivanco, M., Thunis, P., Pay, M.-T., Colette, A., Couvidat, F.,
863 Meleux, F., Rouïl, L., Ung, A., Aksoyoglu, S., Baldasano, J. M., Bieser, J., Briganti, G.,
864 Cappelletti, A., D'Isidoro, M., Finardi, S., Kranenburg, R., Silibello, C., Carnevale, C., Aas,
865 W., Dupont, J.-C., Fagerli, H., Gonzalez, L., Menut, L., Prévôt, A. S. H., Roberts, P., and White,
866 L.: Presentation of the EURODELTA III intercomparison exercise – evaluation of the
867 chemistry transport models' performance on criteria pollutants and joint analysis with
868 meteorology, *Atmospheric Chem. Phys.*, 16, 12667–12701, [https://doi.org/10.5194/acp-16-](https://doi.org/10.5194/acp-16-12667-2016)
869 [12667-2016](https://doi.org/10.5194/acp-16-12667-2016), 2016.
- 870 Carmichael, G. R., Sakurai, T., Streets, D., Hozumi, Y., Ueda, H., Park, S. U., Fung, C., Han, Z.,
871 Kajino, M., Engardt, M., Bennet, C., Hayami, H., Sartelet, K., Holloway, T., Wang, Z., Kannari,
872 A., Fu, J., Matsuda, K., Thongboonchoo, N., and Amann, M.: MICS-Asia II: The model
873 intercomparison study for Asia Phase II methodology and overview of findings, *Atmos.*
874 *Environ.*, 42, 3468–3490, <https://doi.org/10.1016/j.atmosenv.2007.04.007>, 2008.
- 875 Chen, L., Gao, Y., Zhang, M., Fu, J. S., Zhu, J., Liao, H., Li, J., Huang, K., Ge, B., Wang, X., Lam,
876 Y. F., Lin, C.-Y., Itahashi, S., Nagashima, T., Kajino, M., Yamaji, K., Wang, Z., and Kurokawa,
877 J.: MICS-Asia III: multi-model comparison and evaluation of aerosol over East Asia,
878 *Atmospheric Chem. Phys.*, 19, 11911–11937, <https://doi.org/10.5194/acp-19-11911-2019>,
879 2019.
- 880 Colella, P. and Woodward, P. R.: The Piecewise Parabolic Method (PPM) for gas-dynamical
881 simulations, *J. Comput. Phys.*, 54, 174–201, [https://doi.org/10.1016/0021-9991\(84\)90143-8](https://doi.org/10.1016/0021-9991(84)90143-8),
882 1984.
- 883 Crippa, M., Solazzo, E., Huang, G., Guizzardi, D., Koffi, E., Muntean, M., Schieberle, C., Friedrich,
884 R., and Janssens-Maenhout, G.: High resolution temporal profiles in the Emissions Database
885 for Global Atmospheric Research, *Sci. Data*, 7, 121, [https://doi.org/10.1038/s41597-020-0462-](https://doi.org/10.1038/s41597-020-0462-2)
886 [2](https://doi.org/10.1038/s41597-020-0462-2), 2020.
- 887 Emery, C., Jung, J., Johnson, J., Yarwood, G., Madronich, S., Grell, G., and Boyer, D.:
888 IMPROVING CLOUD IMPACTS ON PHOTOLYSIS USING AN ON-LINE RADIATION
889 MODEL IN CAMx, the 9th Annual CMAS Conference, Chapel Hill, NC., 2010.
- 890 Emery, C., Jung, J., Koo, B., and Yarwood, G.: Improvements to CAMx Snow Cover Treatments
891 and Carbon Bond Chemical Mechanism for Winter Ozone, Ramboll Environ, Novato, CA,
892 USA, 2015.
- 893 Emery, C., Baker, K., Wilson, G., and Yarwood, G.: Comprehensive Air Quality Model with
894 Extensions: Formulation and Evaluation for Ozone and Particulate Matter over the US,
895 *Atmosphere*, 15, 1158, <https://doi.org/10.3390/atmos15101158>, 2024.
- 896 EPA:CMAQv5.3.3 User Manual, 2021.
- 897 EPIC-Model Working Group: Description and evaluation of the Emission and atmospheric
898 Processes Integrated and Coupled Community (EPIC) Model version 1.0, *Adv. Atmospheric*
899 *Sci.*, <https://doi.org/10.1007/s00376-025-4384-y>, 2025.
- 900 Fountoukis, C. and Nenes, A.: ISORROPIA II: a computationally efficient thermodynamic
901 equilibrium model for K^+ - Ca^{2+} - Mg^{2+} - NH_4^+ - Na^+ - SO_4^{2-} - NO_3^- - Cl^- - H_2O aerosols.,
902 *Atmospheric Chem. Phys.*, 7, 4639–4659, <https://doi.org/10.5194/acp-7-4639-2007>, 2007.
- 903 Gao, C., Zhang, X., Xiu, A., Tong, Q., Zhao, H., Zhang, S., Yang, G., Zhang, M., and Xie, S.:
904 Intercomparison of multiple two-way coupled meteorology and air quality models (WRF
905 v4.1.1–CMAQ v5.3.1, WRF–Chem v4.1.1, and WRF v3.7.1–CHIMERE v2020r1) in eastern



- 906 China, *Geosci. Model Dev.*, 17, 2471–2492, <https://doi.org/10.5194/gmd-17-2471-2024>, 2024.
- 907 Gao, M., Han, Z., Liu, Z., Li, M., Xin, J., Tao, Z., Li, J., Kang, J.-E., Huang, K., Dong, X., Zhuang,
908 B., Li, S., Ge, B., Wu, Q., Cheng, Y., Wang, Y., Lee, H.-J., Kim, C.-H., Fu, J. S., Wang, T.,
909 Chin, M., Woo, J.-H., Zhang, Q., Wang, Z., and Carmichael, G. R.: Air quality and climate
910 change, Topic 3 of the Model Inter-Comparison Study for Asia Phase III (MICS-Asia III) –
911 Part 1: Overview and model evaluation, *Atmospheric Chem. Phys.*, 18, 4859–4884,
912 <https://doi.org/10.5194/acp-18-4859-2018>, 2018.
- 913 Gao, Y., Yan, F., Ma, M., Ding, A., Liao, H., Wang, S., Wang, X., Zhao, B., Cai, W., Su, H., Yao, X.,
914 and Gao, H.: Unveiling the dipole synergic effect of biogenic and anthropogenic emissions on
915 ozone concentrations, *Sci. Total Environ.*, 818, 151722,
916 <https://doi.org/10.1016/j.scitotenv.2021.151722>, 2022.
- 917 Gao, Z. and Zhou, X.: A review of the CAMx, CMAQ, WRF-Chem and NAQPMS models:
918 Application, evaluation and uncertainty factors, *Environ. Pollut.*, 343, 123183,
919 <https://doi.org/10.1016/j.envpol.2023.123183>, 2024.
- 920 Geng, G., Liu, Y., Liu, Y., Liu, S., Cheng, J., Yan, L., Wu, N., Hu, H., Tong, D., Zheng, B., Yin, Z.,
921 He, K., and Zhang, Q.: Efficacy of China’s clean air actions to tackle PM_{2.5} pollution between
922 2013 and 2020, *Nat. Geosci.*, 17, 987–994, <https://doi.org/10.1038/s41561-024-01540-z>, 2024.
- 923 Gong, C. and Liao, H.: A typical weather pattern for ozone pollution events in North China,
924 *Atmospheric Chem. Phys.*, 19, 13725–13740, <https://doi.org/10.5194/acp-19-13725-2019>,
925 2019.
- 926 Guenther, A. B., Jiang, X., Heald, C. L., Sakulyanontvittaya, T., Duhl, T., Emmons, L. K., and Wang,
927 X.: The Model of Emissions of Gases and Aerosols from Nature version 2.1 (MEGAN2.1): an
928 extended and updated framework for modeling biogenic emissions, *Geosci. Model Dev.*, 5,
929 1471–1492, <https://doi.org/10.5194/gmd-5-1471-2012>, 2012.
- 930 Hong, C., Zhang, Q., He, K., Guan, D., Li, M., Liu, F., and Zheng, B.: Variations of China’s emission
931 estimates: response to uncertainties in energy statistics, *Atmospheric Chem. Phys.*, 17, 1227–
932 1239, <https://doi.org/10.5194/acp-17-1227-2017>, 2017.
- 933 Hong, S.-Y., Noh, Y., and Dudhia, J.: A New Vertical Diffusion Package with an Explicit Treatment
934 of Entrainment Processes, *Mon. Weather Rev.*, 134, 2318–2341,
935 <https://doi.org/10.1175/MWR3199.1>, 2006.
- 936 Hu, X.-M., Nielsen-Gammon, J. W., and Zhang, F.: Evaluation of Three Planetary Boundary Layer
937 Schemes in the WRF Model, *J. Appl. Meteorol. Climatol.*, 49, 1831–1844,
938 <https://doi.org/10.1175/2010JAMC2432.1>, 2010.
- 939 Huang, L., Zhu, Y., Zhai, H., Xue, S., Zhu, T., Shao, Y., Liu, Z., Emery, C., Yarwood, G., Wang, Y.,
940 Fu, J., Zhang, K., and Li, L.: Recommendations on benchmarks for numerical air quality model
941 applications in China – Part 1: PM_{2.5} and chemical species, *Atmospheric Chem. Phys.*, 21,
942 2725–2743, <https://doi.org/10.5194/acp-21-2725-2021>, 2021.
- 943 Huang, L., Liu, H., Yarwood, G., Wilson, G., Tao, J., Han, Z., Ji, D., Wang, Y., and Li, L.: Modeling
944 of secondary organic aerosols (SOA) based on two commonly used air quality models in China:
945 Consistent S/IVOCs contribution but large differences in SOA aging, *Sci. Total Environ.*, 903,
946 166162, <https://doi.org/10.1016/j.scitotenv.2023.166162>, 2023.
- 947 Huang, X., Song, Y., Li, M., Li, J., Huo, Q., Cai, X., Zhu, T., Hu, M., and Zhang, H.: A high-
948 resolution ammonia emission inventory in China, *Glob. Biogeochem. Cycles*, 26,
949 <https://doi.org/10.1029/2011GB004161>, 2012a.



- 950 Huang, X., Li, M., Li, J., and Song, Y.: A high-resolution emission inventory of crop burning in
951 fields in China based on MODIS Thermal Anomalies/Fire products, *Atmos. Environ.*, 50, 9–
952 15, <https://doi.org/10.1016/j.atmosenv.2012.01.017>, 2012b.
- 953 Iacono, M. J., Delamere, J. S., Mlawer, E. J., Shephard, M. W., Clough, S. A., and Collins, W. D.:
954 Radiative forcing by long-lived greenhouse gases: Calculations with the AER radiative transfer
955 models, *J. Geophys. Res. Atmospheres*, 113, <https://doi.org/10.1029/2008JD009944>, 2008.
- 956 Itahashi, S., Ge, B., Sato, K., Fu, J. S., Wang, X., Yamaji, K., Nagashima, T., Li, J., Kajino, M., Liao,
957 H., Zhang, M., Wang, Z., Li, M., Kurokawa, J., Carmichael, G. R., and Wang, Z.: MICS-Asia
958 III: overview of model intercomparison and evaluation of acid deposition over Asia,
959 *Atmospheric Chem. Phys.*, 20, 2667–2693, <https://doi.org/10.5194/acp-20-2667-2020>, 2020.
- 960 Jia, W. and Zhang, X.: The role of the planetary boundary layer parameterization schemes on the
961 meteorological and aerosol pollution simulations: A review, *Atmospheric Res.*, 239, 104890,
962 <https://doi.org/10.1016/j.atmosres.2020.104890>, 2020.
- 963 Jia, W., Zhang, X., Wang, H., Wang, Y., Wang, D., Zhong, J., Zhang, W., Zhang, L., Guo, L., Lei,
964 Y., Wang, J., Yang, Y., and Lin, Y.: Comprehensive evaluation of typical planetary boundary
965 layer (PBL) parameterization schemes in China – Part I: Understanding expressiveness of
966 schemes for different regions from the mechanism perspective, *Geosci. Model Dev.*, 16, 6635–
967 6670, <https://doi.org/10.5194/gmd-16-6635-2023>, 2023.
- 968 Jiang, F., Guo, H., Wang, T. J., Cheng, H. R., Wang, X. M., Simpson, I. J., Ding, A. J., Saunders, S.
969 M., Lam, S. H. M., and Blake, D. R.: An ozone episode in the Pearl River Delta: Field
970 observation and model simulation, *J. Geophys. Res. Atmospheres*, 115, 2009JD013583,
971 <https://doi.org/10.1029/2009JD013583>, 2010.
- 972 Jiménez, P. A. and Dudhia, J.: On the Ability of the WRF Model to Reproduce the Surface Wind
973 Direction over Complex Terrain, *J. Appl. Meteorol. Climatol.*, 52, 1610–1617,
974 <https://doi.org/10.1175/JAMC-D-12-0266.1>, 2013.
- 975 Jing, Z., Liu, P., Wang, T., Song, H., Lee, J., Xu, T., and Xing, Y.: Effects of Meteorological Factors
976 and Anthropogenic Precursors on PM_{2.5} Concentrations in Cities in China, *Sustainability*, 12,
977 3550, <https://doi.org/10.3390/su12093550>, 2020.
- 978 Kain, J. S.: The Kain–Fritsch Convective Parameterization: An Update, *J. Appl. Meteorol.*, 43, 170–
979 181, [https://doi.org/10.1175/1520-0450\(2004\)043%253C0170:TKCPAU%253E2.0.CO;2](https://doi.org/10.1175/1520-0450(2004)043%253C0170:TKCPAU%253E2.0.CO;2),
980 2004.
- 981 Kang, Y., Liu, M., Song, Y., Huang, X., Yao, H., Cai, X., Zhang, H., Kang, L., Liu, X., Yan, X., He,
982 H., Zhang, Q., Shao, M., and Zhu, T.: High-resolution ammonia emissions inventories in China
983 from 1980 to 2012, *Atmospheric Chem. Phys.*, 16, 2043–2058, <https://doi.org/10.5194/acp-16-2043-2016>, 2016.
- 985 Kim, D.-J., Kim, T.-H., Choi, J.-Y., Lee, J., Kim, R.-H., Son, J.-S., and Lee, D.: The Impact of
986 Vertical Eddy Diffusivity Changes in the CMAQ Model on PM_{2.5} Concentration Variations in
987 Northeast Asia: Focusing on the Seoul Metropolitan Area, *Atmosphere*, 15, 376,
988 <https://doi.org/10.3390/atmos15030376>, 2024.
- 989 Kong, L., Tang, X., Zhu, J., Wang, Z., Pan, Y., Wu, H., Wu, L., Wu, Q., He, Y., Tian, S., Xie, Y., Liu,
990 Z., Sui, W., Han, L., and Carmichael, G.: Improved Inversion of Monthly Ammonia Emissions
991 in China Based on the Chinese Ammonia Monitoring Network and Ensemble Kalman Filter,
992 *Environ. Sci. Technol.*, 53, 12529–12538, <https://doi.org/10.1021/acs.est.9b02701>, 2019.
- 993 Li, J., Nagashima, T., Kong, L., Ge, B., Yamaji, K., Fu, J. S., Wang, X., Fan, Q., Itahashi, S., Lee,



- 994 H.-J., Kim, C.-H., Lin, C.-Y., Zhang, M., Tao, Z., Kajino, M., Liao, H., Li, M., Woo, J.-H.,
995 Kurokawa, J., Wang, Z., Wu, Q., Akimoto, H., Carmichael, G. R., and Wang, Z.: Model
996 evaluation and intercomparison of surface-level ozone and relevant species in East Asia in the
997 context of MICS-Asia Phase III – Part 1: Overview, *Atmospheric Chem. Phys.*, 19, 12993–
998 13015, <https://doi.org/10.5194/acp-19-12993-2019>, 2019a.
- 999 Li, K., Jacob, D. J., Liao, H., Zhu, J., Shah, V., Shen, L., Bates, K. H., Zhang, Q., and Zhai, S.: A
1000 two-pollutant strategy for improving ozone and particulate air quality in China, *Nat. Geosci.*,
1001 12, 906–910, <https://doi.org/10.1038/s41561-019-0464-x>, 2019b.
- 1002 Li, R., Ma, X., Xiong, F., Jia, H., Sha, T., and Tian, R.: Comparisons and evaluation of aerosol
1003 burden and optical depth in CMIP5 simulations over East Asia, *J. Atmospheric Sol.-Terr. Phys.*,
1004 206, 105315, <https://doi.org/10.1016/j.jastp.2020.105315>, 2020.
- 1005 Li, X., Hussain, S. A., Sobri, S., and Md Said, M. S.: Overiewing the air quality models on air
1006 pollution in Sichuan Basin, China, *Chemosphere*, 271, 129502,
1007 <https://doi.org/10.1016/j.chemosphere.2020.129502>, 2021.
- 1008 Liu, Z., Zhou, M., Chen, Y., Chen, D., Pan, Y., Song, T., Ji, D., Chen, Q., and Zhang, L.: The
1009 nonlinear response of fine particulate matter pollution to ammonia emission reductions in
1010 North China, *Environ. Res. Lett.*, <https://doi.org/10.1088/1748-9326/abdf86>, 2021.
- 1011 Lou, M., Wu, Q., Li, J., Cheng, H., Zhu, J., Wang, L., and Wang, Z.: The amplification effect of El
1012 Niño on winter heavy pollution frequency in Beijing, *Environ. Res. Lett.*, 20, 074043,
1013 <https://doi.org/10.1088/1748-9326/ade1ee>, 2025.
- 1014 Lyu, Y., Wu, D., Han, F., Zhang, H., Lv, F., Kang, A., Hu, Y., and Pang, X.: Co-Occurring Extremes
1015 of PM_{2.5} and Ozone in Warm Seasons of the Yangtze River Delta of China: Insights from
1016 Explainable Machine Learning, *ACS EST Air*, 2, 578–588,
1017 <https://doi.org/10.1021/acsestair.4c00314>, 2025.
- 1018 Miao, R., Chen, Q., Zheng, Y., Cheng, X., Sun, Y., Palmer, P. I., Shrivastava, M., Guo, J., Zhang,
1019 Q., Liu, Y., Tan, Z., Ma, X., Chen, S., Zeng, L., Lu, K., and Zhang, Y.: Model bias in simulating
1020 major chemical components of PM_{2.5} in China, *Atmospheric Chem. Phys.*, 20, 12265–12284,
1021 <https://doi.org/10.5194/acp-20-12265-2020>, 2020.
- 1022 Murphy, B. N., Woody, M. C., Jimenez, J. L., Carlton, A. M. G., Hayes, P. L., Liu, S., Ng, N. L.,
1023 Russell, L. M., Setyan, A., Xu, L., Young, J., Zaveri, R. A., Zhang, Q., and Pye, H. O. T.:
1024 Semivolatile POA and parameterized total combustion SOA in CMAQv5.2: impacts on source
1025 strength and partitioning, *Atmospheric Chem. Phys.*, 17, 11107–11133,
1026 <https://doi.org/10.5194/acp-17-11107-2017>, 2017.
- 1027 NASA: Tropospheric ultraviolet and visible (TUV) radiation model.
1028 [https://www2.acom.ucar.edu/modeling/tropospheric-ultraviolet-and-visible-tuv-radiation-](https://www2.acom.ucar.edu/modeling/tropospheric-ultraviolet-and-visible-tuv-radiation-model)
1029 [model](https://www2.acom.ucar.edu/modeling/tropospheric-ultraviolet-and-visible-tuv-radiation-model) (2024), Accessed 12th Feb 2026.
- 1030 NCEP: NCEP FNL Operational Model Global Tropospheric Analyses, continuing from July 1999,
1031 National Centers for Environmental Prediction [data set], <https://doi.org/10.5065/D6M043C6>,
1032 2000.
- 1033 Nenes, A., Pandis, S. N., and Pilinis, C.: ISORROPIA: A New Thermodynamic Equilibrium Model
1034 for Multiphase Multicomponent Inorganic Aerosols, *Aquat. Geochem.*, 4, 123–152,
1035 <https://doi.org/10.1023/A:1009604003981>, 1998.
- 1036 Odum, J. R., W, J. T. P., C, F. R., and H, S. J.: The Atmospheric Aerosol-Forming Potential of Whole
1037 Gasoline Vapor., *Science*, 276, 96–99, 1997.



- 1038 Oyegbile, O., Chan, A., Ooi, M., Anwar, P., Mohamed, A. A., and Li, L.: Evaluation of WRF model
1039 performance with different microphysics schemes for extreme rainfall prediction in Lagos,
1040 Nigeria: Implications for urban flood risk management, *Bull. Atmospheric Sci. Technol.*, 5, 19,
1041 <https://doi.org/10.1007/s42865-024-00081-y>, 2024.
- 1042 Pandis, S. N., Harley, R. A., Cass, G. R., and Seinfeld, J. H.: Secondary organic aerosol formation
1043 and transport, *Atmos. Environ.*, 26, 2269–2282, [https://doi.org/10.1016/0960-1686\(92\)90358-](https://doi.org/10.1016/0960-1686(92)90358-r)
1044 [r](https://doi.org/10.1016/0960-1686(92)90358-r), 1992.
- 1045 Pennington, E. A., Seltzer, K. M., Murphy, B. N., Qin, M., Seinfeld, J. H., and Pye, H. O. T.:
1046 Modeling secondary organic aerosol formation from volatile chemical products, *Atmospheric*
1047 *Chem. Phys.*, 21, 18247–18261, <https://doi.org/10.5194/acp-21-18247-2021>, 2021.
- 1048 Pleim, J. E.: A Combined Local and Nonlocal Closure Model for the Atmospheric Boundary Layer.
1049 Part I: Model Description and Testing, *J. Appl. Meteorol. Climatol.*, 46, 1383–1395,
1050 <https://doi.org/10.1175/JAM2539.1>, 2007.
- 1051 Ramboll: CAMx User’s Guide v7.00, 2020. Ren, F., Lin, J., Xu, C., Adeniran, J. A., Wang, J., Martin,
1052 R. V., van Donkelaar, A., Hammer, M. S., Horowitz, L. W., Turnock, S. T., Oshima, N., Zhang,
1053 J., Bauer, S., Tsigaridis, K., Seland, Ø., Nabat, P., Neubauer, D., Strand, G., van Noije, T., Le
1054 Sager, P., and Takemura, T.: Evaluation of CMIP6 model simulations of PM_{2.5} and its
1055 components over China, *Geosci. Model Dev.*, 17, 4821–4836, [https://doi.org/10.5194/gmd-17-](https://doi.org/10.5194/gmd-17-4821-2024)
1056 [4821-2024](https://doi.org/10.5194/gmd-17-4821-2024), 2024.
- 1057 Ren, J., Guo, F., and Xie, S.: Diagnosing ozone–NO_x–VOC sensitivity and revealing causes of ozone
1058 increases in China based on 2013–2021 satellite retrievals, *Atmospheric Chem. Phys.*, 22,
1059 15035–15047, <https://doi.org/10.5194/acp-22-15035-2022>, 2022.
- 1060 Seinfeld, J. H. and Pandis, S. N.: *Atmospheric Chemistry and Physics: From Air Pollution to*
1061 *Climate Change*, 3rd Edition, Wiley, 2016.
- 1062 Shao, J., Chen, Q., Wang, Y., Lu, X., He, P., Sun, Y., Shah, V., Martin, R. V., Philip, S., Song, S.,
1063 Zhao, Y., Xie, Z., Zhang, L., and Alexander, B.: Heterogeneous sulfate aerosol formation
1064 mechanisms during wintertime Chinese haze events: air quality model assessment using
1065 observations of sulfate oxygen isotopes in Beijing, *Atmospheric Chem. Phys.*, 19, 6107–6123,
1066 <https://doi.org/10.5194/acp-19-6107-2019>, 2019.
- 1067 Shi, L., Zhu, A., Huang, L., Yaluk, E., Gu, Y., Wang, Y., Wang, S., Chan, A., and Li, L.: Impact of
1068 the planetary boundary layer on air quality simulations over the Yangtze River Delta region,
1069 China, *Atmos. Environ.*, 263, 118685, <https://doi.org/10.1016/j.atmosenv.2021.118685>, 2021.
- 1070 Sillman, S.: The relation between ozone, NO_x and hydrocarbons in urban and polluted rural
1071 environments, *Atmos. Environ.*, 33, 1821–1845, [https://doi.org/10.1016/S1352-](https://doi.org/10.1016/S1352-2310(98)00345-8)
1072 [2310\(98\)00345-8](https://doi.org/10.1016/S1352-2310(98)00345-8), 1999.
- 1073 Skamarock, W. C., Klemp, J. B., Dudhia, J., Gill, D. O., Barker, D., Duda, M. G., Huang, X. Y.,
1074 Wang, W., and Powers, J. G.: A description of the Advanced Research WRF version 3, NCAR
1075 Technical note-475+ STR, <https://doi.org/10.5065/D68S4MVH>, 2008.
- 1076 Song, Y., Liu, B., Miao, W., Chang, D., and Zhang, Y.: Spatiotemporal variation in nonagricultural
1077 open fire emissions in China from 2000 to 2007, *Glob. Biogeochem. Cycles*, 23,
1078 2008GB003344, <https://doi.org/10.1029/2008GB003344>, 2009.
- 1079 Tang, W., Cohan, D. S., Morris, G. A., Byun, D. W., and Luke, W. T.: Influence of vertical mixing
1080 uncertainties on ozone simulation in CMAQ, *Atmos. Environ.*, 45, 2898–2909,
1081 <https://doi.org/10.1016/j.atmosenv.2011.01.057>, 2011.



- 1082 Tewari, M., Chen, F., Wang, W., Dudhia, J., LeMone, M. A., Gayno, G., Wegiel, J., and Cuenca, R.
1083 H.: A IMPLEMENTATION AND VERIFICATION OF THE UNIFIED NOAH LAND
1084 SURFACE MODEL IN THE WRF MODEL, 20th Conf. Weather Anal. Forecast. Conf. Numer.
1085 Weather Predict., 11–15, 2004.
- 1086 Thompson, G., Field, P. R., Rasmussen, R. M., and Hall, W. D.: Explicit Forecasts of Winter
1087 Precipitation Using an Improved Bulk Microphysics Scheme. Part II: Implementation of a New
1088 Snow Parameterization, *Mon. Weather Rev.*, 136, 5095–5115,
1089 <https://doi.org/10.1175/2008MWR2387.1>, 2008.
- 1090 US EPA: CMAQ, <https://doi.org/10.5281/zenodo.5213949>, 2021.
- 1091 Walcek, C. J. and Aleksic, N. M.: A simple but accurate mass conservative, peak-preserving, mixing
1092 ratio bounded advection algorithm with FORTRAN code, *Atmos. Environ.*, 32, 3863–3880,
1093 [https://doi.org/10.1016/S1352-2310\(98\)00099-5](https://doi.org/10.1016/S1352-2310(98)00099-5), 1998.
- 1094 Walcek, C. J. and Taylor, G. R.: A Theoretical Method for Computing Vertical Distributions of
1095 Acidity and Sulfate Production within Cumulus Clouds, *J. Atmospheric Sci.*, 43, 339–355,
1096 1986.
- 1097 Wang, H., Lu, X., Palmer, P. I., Zhang, L., Lu, K., Li, K., Nagashima, T., Koo, J.-H., Tanimoto, H.,
1098 Wang, H., Gao, M., He, C., Wu, K., Fan, S., and Zhang, Y.: Deciphering decadal urban ozone
1099 trends from historical records since 1980, *Natl. Sci. Rev.*, 11, nwae369,
1100 <https://doi.org/10.1093/nsr/nwae369>, 2024.
- 1101 Wang, W., Li, X., Shao, M., Hu, M., Zeng, L., Wu, Y., and Tan, T.: The impact of aerosols on
1102 photolysis frequencies and ozone production in Beijing during the 4-year period 2012–2015,
1103 *Atmospheric Chem. Phys.*, 19, 9413–9429, <https://doi.org/10.5194/acp-19-9413-2019>, 2019.
- 1104 Wang, W., Liu, M., Wang, T., Song, Y., Zhou, L., Cao, J., Hu, J., Tang, G., Chen, Z., Li, Z., Xu, Z.,
1105 Peng, C., Lian, C., Chen, Y., Pan, Y., Zhang, Y., Sun, Y., Li, W., Zhu, T., Tian, H., and Ge, M.:
1106 Sulfate formation is dominated by manganese-catalyzed oxidation of SO₂ on aerosol surfaces
1107 during haze events, *Nat. Commun.*, 12, 1993, <https://doi.org/10.1038/s41467-021-22091-6>,
1108 2021.
- 1109 Wang, W., Chen, H., Wang, Z., Li, J., Chen, X., Yu, F., Fan, X., Zhao, S., Hu, B., Wang, W., Tang,
1110 X., Wang, Z., Ge, B., and Wu, J.: Development and evaluation of photolysis and gas-phase
1111 reaction scheme in EPIC-model: Impacts on tropospheric ozone simulation, *Atmos. Environ.*,
1112 359, 121373, <https://doi.org/10.1016/j.atmosenv.2025.121373>, 2025.
- 1113 Wang, X., Zhang, Y., Hu, Y., Zhou, W., Lu, K., Zhong, L., Zeng, L., Shao, M., Hu, M., and Russell,
1114 A. G.: Process analysis and sensitivity study of regional ozone formation over the Pearl River
1115 Delta, China, during the PRIDE-PRD2004 campaign using the Community Multiscale Air
1116 Quality modeling system, *Atmospheric Chem. Phys.*, 10, 4423–4437,
1117 <https://doi.org/10.5194/acp-10-4423-2010>, 2010.
- 1118 Wang, Y., Jiang, S., Huang, L., Lu, G., Kasemsan, M., Yaluk, E. A., Liu, H., Liao, J., Bian, J., Zhang,
1119 K., Chen, H., and Li, L.: Differences between VOCs and NO_x transport contributions, their
1120 impacts on O₃, and implications for O₃ pollution mitigation based on CMAQ simulation over
1121 the Yangtze River Delta, China, *Sci. Total Environ.*, 872, 162118,
1122 <https://doi.org/10.1016/j.scitotenv.2023.162118>, 2023.
- 1123 Wild, O., Zhu, X., and Prather, M. J.: Fast-J: Accurate Simulation of In- and Below-Cloud
1124 Photolysis in Tropospheric Chemical Models, *J. Atmospheric Chem.*, 37, 245–282, 2000.
- 1125 William, H.: III. Experiments on the quantity of gases absorbed by water, at different temperatures,



- 1126 and under different pressures, *Philos. Trans. R. Soc. Lond.*,
1127 <https://doi.org/10.1098/rstl.1803.0004>, 1803.
- 1128 Wu, Q., Wang, Z., Chen, H., Zhou, W., and Wenig, M.: An evaluation of air quality modeling over
1129 the Pearl River Delta during November 2006, *Meteorol. Atmospheric Phys.*, 116, 113–132,
1130 <https://doi.org/10.1007/s00703-011-0179-z>, 2012.
- 1131 Xiao, Q., Geng, G., Xue, T., Liu, S., Cai, C., He, K., and Zhang, Q.: Tracking PM_{2.5} and O₃
1132 Pollution and the Related Health Burden in China 2013–2020, *Environ. Sci. Technol.*, 56,
1133 6922–6932, <https://doi.org/10.1021/acs.est.1c04548>, 2022.
- 1134 Xu, W., Ning, L., and Luo, Y.: Applying Satellite Data Assimilation to Wind Simulation of Coastal
1135 Wind Farms in Guangdong, China, *Remote Sens.*, 12, 973, <https://doi.org/10.3390/rs12060973>,
1136 2020.
- 1137 Yang, J., Qu, Y., Chen, Y., Zhang, J., Liu, X., Niu, H., and An, J.: Dominant physical and chemical
1138 processes impacting nitrate in Shandong of the North China Plain during winter haze events,
1139 *Sci. Total Environ.*, 912, 169065, <https://doi.org/10.1016/j.scitotenv.2023.169065>, 2024.
- 1140 Yarwood, G., Yocke, S. R. M., and Whitten, G.: Updates to the Carbon Bond Mechanism: CB05,
1141 U.S. Environmental Protection Agency, 2005.
- 1142 Yarwood, G., Beardsley, R., and Shi, Y.: Revision 5 of the Carbon Bond 6 Mechanism (CB6r5),
1143 2020.
- 1144 Yu, E., Ma, J., and Sun, J.: Developing a Climate Prediction System over Southwest China Using
1145 the 8-km Weather Research and Forecasting (WRF) Model: System Design, Model Calibration,
1146 and Performance Evaluation, *Weather Forecast.*, 37, 1703–1719, [https://doi.org/10.1175/WAF-](https://doi.org/10.1175/WAF-D-21-0188.1)
1147 [D-21-0188.1](https://doi.org/10.1175/WAF-D-21-0188.1), 2022a.
- 1148 Yu, E., Bai, R., Chen, X., and Shao, L.: Impact of physical parameterizations on wind simulation
1149 with WRF V3.9.1.1 under stable conditions at planetary boundary layer gray-zone resolution:
1150 a case study over the coastal regions of North China, *Geosci. Model Dev.*, 15, 8111–8134,
1151 <https://doi.org/10.5194/gmd-15-8111-2022>, 2022b.
- 1152 Zhang, J., Lian, C., Wang, W., Ge, M., Guo, Y., Ran, H., Zhang, Y., Zheng, F., Fan, X., Yan, C.,
1153 Daellenbach, K. R., Liu, Y., Kulmala, M., and An, J.: Amplified role of potential HONO
1154 sources in O₃ formation in North China Plain during autumn haze aggravating processes,
1155 *Atmospheric Chem. Phys.*, 22, 3275–3302, <https://doi.org/10.5194/acp-22-3275-2022>, 2022.
- 1156 Zhang, L., Gong, S., Padro, J., and Barrie, L.: A size-segregated particle dry deposition scheme for
1157 an atmospheric aerosol module, *Atmos. Environ.*, 35, 549–560, [https://doi.org/10.1016/S1352-](https://doi.org/10.1016/S1352-2310(00)00326-5)
1158 [2310\(00\)00326-5](https://doi.org/10.1016/S1352-2310(00)00326-5), 2001.
- 1159 Zhang, L., Brook, J. R., and Vet, R.: A revised parameterization for gaseous dry deposition in air-
1160 quality models, *Atmospheric Chem. Phys.*, 3, 2067–2082, [https://doi.org/10.5194/acp-3-2067-](https://doi.org/10.5194/acp-3-2067-2003)
1161 [2003](https://doi.org/10.5194/acp-3-2067-2003), 2003.
- 1162 Zhang, X. Y., Wang, Y. Q., Niu, T., Zhang, X. C., Gong, S. L., Zhang, Y. M., and Sun, J. Y.:
1163 Atmospheric aerosol compositions in China: spatial/temporal variability, chemical signature,
1164 regional haze distribution and comparisons with global aerosols, *Atmospheric Chem. Phys.*,
1165 12, 779–799, <https://doi.org/10.5194/acp-12-779-2012>, 2012.
- 1166 Zhu, Q., Yu, Y., Gong, H., Wang, Y., Wang, H., Wang, W., Xu, B., and Cheng, T.: Spatio-temporal
1167 characteristics of PM_{2.5} and O₃ synergic pollutions and influence factors in the Yangtze River
1168 Delta, *Front. Environ. Sci.*, <https://doi.org/10.3389/fenvs.2022.1104013>, 2023.
- 1169
- 1170